Journal of the European Ceramic Society 21 (2001) 2541–2562

www.elsevier.com/locate/jeurceramsoc

Crystal structure development during devitrification of quenched mullite

Bradley R. Johnson[a,*,1], Waltraud M. Kriven[a], Julius Schneider[b]

[a]*Department of Materials Science and Engineering, University of Illinois at Urbana-Champaign, Urbana, IL 61801, USA*
[b]*Institut für Kristallographie und Angewandte Mineralogie, Ludwig Maximilians Universität, München, Germany*

Abstract

The kinetics, microstructural changes, and crystal structure development for crystallization of amorphous, quenched, mullite composition glass ($3Al_2O_3{\cdot}2SiO_2$) were studied between 900 and 1400°C. The phenomena observed were characterized using non-isothermal differential scanning calorimetry (DSC), transmission electron microscopy (TEM), energy dispersive spectroscopy (EDS), powder X-ray diffraction (XRD, with both a standard laboratory diffractometer, as well as with synchrotron radiation), and Rietveld analysis. Crystallization of amorphous mullite was observed to occur in two steps. The activation energy for crystallization was 892 kJ/mol for the first step and 1333 kJ/mol for the second step. From the amorphous state, the first phase(s) to crystallize were alumina-rich, pseudotetragonal mullite (~70 mol% Al_2O_3). These crystals were highly strained and contained numerous nanometer scale inclusions. With increasing temperature, the crystals were observed to incorporate increasing amounts of SiO_2, and approach the equilibrium orthorhombic structure. By 1400°C the pseudotetragonal to orthorhombic transition was complete, the strain was eliminated, most of the inclusions had been assimilated, there was ~67% reduction in grain size, and the crystals had attained the composition of the initial, bulk glass (~60 mol% Al_2O_3).

Keywords: Crystallization; Kinetics; Microstructure; Mullite; Rietveld

1. Introduction

Mullite ($3Al_2O_3{\cdot}2SiO_2$) is the only stable compound in the Al_2O_3–SiO_2 phase diagram at ambient pressures. It occurs in a narrow, temperature-dependent, solid solution range, between ~58 and 63 mol% Al_2O_3.[1–3] It is an important structural and refractory ceramic with very good strength and creep properties. It is often used in such application as refractory bricks, furnace liners, and for structural fibers. Considerable work has been done to characterize the composition and structure of mullite.

The equilibrium crystal structure of mullite with a composition of $3Al_2O_3{\cdot}2SiO_2$, (60 mol% Al_2O_3) is orthorhombic, and it belongs to the space group Pbam.[4–7] However, the composition and crystal structure of mullite varies with the formation temperature. When formed from molecularly mixed precursors at temperatures less than 1200°C, the first mullite crystals formed tend to be Al_2O_3-rich (~70 mol% Al_2O_3) independent of the bulk composition of the precursors.[8] These crystals have an a-lattice parameter that is very close in size to their b-lattice parameter. The correlation between the variation in the lattice parameters with the composition of mullite was initially reported by Cameron,[9] and subsequently verified and refined by Kriven and Pask,[1] Okada and Otsuka,[3] Ban and Okada[10] and Fischer et al.[11,12] This initial crystal structure with a≈b has sometimes been termed pseudotetragonal mullite)[10,13–15] Another way to describe the structure is to call it the "pseudotetragonal metric",[16] since the crystal symmetry is still orthorhombic even when the a-lattice and b-lattice parameters are equal in length. Although termed pseudotetragonal, there is only a very subtle difference between the pseudotetragonal metric and orthorhombic mullite. This distinction can be observed by close examination of the extent of splitting between the (120) and (210) peaks at approximately 26° 2θ (using CuK_α radiation). When initially formed, the two peaks overlap for the pseudotetragonal metric, and as the annealing temperature increases, the peaks gradually split apart and become more distinct ($d_{120}=3.428$ Å, $d_{210}=3.390$ Å, powder diffraction file 15-776).[14,17] This structural change with increase in temperature was interpreted as incorporation of SiO_2 into the mullite structure, resulting in the reduction of the a-lattice parameter.[3,18]

* Corresponding author

[1] Present address: Pacific Northwest Laboratory, P.O. Box 999, K6-24, Richland, WA 99352, USA.

0955-2219/01/$ - see front matter
PII: S0955-2219(01)00268-0

An anomaly of the gradual compositional and structural change in mullite as it crystallizes, is the variation in the c-lattice parameter. Although the "a" and "b" lattice parameters change linearly with composition, (and hence with temperature as precursors crystallize), the value and the variation of the c-lattice parameter depends on the initial formation temperature. Mullite crystals of a given composition formed at temperatures below 1200°C have c-lattice parameters that are approximately 0.0005 nm shorter than mullite crystals of the same composition that were heated above 1200°C. This variation was first pointed out by Ban and Okada,[10,19] but the same trend can be observed in data previously presented by Okada et al.[3,18]

Considerable work has been done regarding the crystallization of amorphous mullite precursors.[20–23] Depending on the degree of homogeneity, two primary crystallization pathways appear to be most prominent. In the case of molecularly mixed precursors (such as a slowly hydrolyzed sol-gel precursor, or an amorphous glass) mullite crystallizes between approx. 920–1000°C, depending on the heating rate.[18] For inhomogeneously mixed systems (e.g. kaolinite, diphasic precursors, or rapidly hydrolyzed gels) intermediate phases such as spinel ($6Al_2O_3{\cdot}SiO_2$) form around 1000°C, and are subsequently converted to mullite around 1200°C.[24–29] For chemically synthesized mullite, the processing conditions play a critical role in obtaining single-phase, molecularly mixed precursors, and great care is necessary to avoid forming diphasic precursors.[30]

Recently, work has been done to synthesize structural mullite fibers drawn from the melt using containerless methods.[31–33] These amorphous fibers require subsequent thermal processing to crystallize them. The crystallization of quenched, amorphous mullite composition glasses was studied to determine appropriate processing conditions for the crystallization of melt-drawn, mullite composition, fibers. This work was focused on gaining greater understanding of the kinetics, microstructural changes, and crystal structure development during crystallization of quenched, amorphous, mullite composition, glass.

2. Experimental procedures

2.1. Materials

Commercially obtained mullite powder (KM 101 mullite powder, Kyoritsu Ceramic Materials Co. Ltd., Nagoya, Japan) was supplied to Containerless Research Inc. (Evanston, IL) for processing to synthesize amorphous beads and fibers. The powders were melted in a water-cooled hearth using a CO_2 laser to form a spherical bead.[34] The bead was then levitated in an oxygen atmosphere with an aero-acoustic levitator, and melted again with a CO_2 laser as described in literature elsewhere.[35–38] Melt temperatures were approximately 2200°C as indicated by optical pyrometry. Amorphous beads were formed by rapidly quenching the levitated molten droplet at a rate of approximately 250°C/s. The solid beads were about 2–3 mm in diameter. They were subsequently crushed between two stainless steel plates to form a coarse powder. Final grinding was accomplished with an agate mortar and pestle, to produce a fine powder that was used in thermal analysis, X-ray diffraction, and TEM experiments.

2.2. Thermal analysis

Nucleation and crystallization studies of as-received, ground, quenched, mullite composition beads were conducted with a Netzsch STA 409 Simultaneous Thermal Analyzer (Selb, Germany) used in DSC mode. The experiments were done in a flowing atmosphere of 75 cc/mm of Ar. Covered Pt crucibles to were used to hold the specimen and the reference (α-alumina), and a mass of ~15.0 mg was used for each. Temperature calibration of the instrument was accomplished by observing the melting points of 99.999% gold and silver. The average value of three different melting points was used.

Two different types of experiments were used to study the nucleation and crystallization of amorphous, mullite composition glasses. Nucleation experiments were conducted to determine the effects of pre-crystallization heat treatment on the crystallization temperature, T_p (the temperature at the maximum of the crystallization exotherm). The specimens were heated at 20°C/min to a specified soak (or nucleation) temperature (T_N), annealed at that temperature for 3 h, and then heated again at a 10°C/min to a maximum temperature of 1100°C. The variation in crystallization temperature, T_p, during the second heating ramp was observed. This was repeated for a series of different nucleation temperatures (850–940°C). This information was necessary to set up conditions for the second set of experiments.

Non-isothermal DSC experiments were used to determine the crystallization kinetics of amorphous mullite composition glass beads. The specimens were heated at a rate of 20°C/min to 850°C, and held there for 15 min. Above that temperature, 10 different heating rates were used (viz. 0.5, 1.0, 1.5, 2.0, 3.0, 4.0, 5.0, 6.0, 8.0 and 10.0°C/min) to heat the specimen up to a maximum temperature of 1100°C. Crystallization was observed to occur exothermally during the second heating ramp segment. The variation in T_p with heating rate was used to calculate the kinetics of crystallization.

2.3. Electron microscopy

The microstructure and microchemical composition of mullite at various stages of crystallization were characterized using a TEM (Philips CM12, FEI Company,

Hillsboro, OR, USA) equipped with an EDS detector (EDAX, Mahwah, NJ, USA). Selected specimens were also examined with a Vacuum Generators HB 501 scanning transmission electron microscope (STEM) equipped with a 100 kV field emission gun filament and an Oxford Instruments (Oxfordshire, England) Link® EDS system. Several different specimens were chosen after being subjected to various thermal treatments (Table 1). Specimens were prepared from ground, quenched, mullite composition beads as well as from tripod polished,[39,40] and ion milled sliced sections of quenched beads. The specimens were examined by bright field (BF) and dark field (DF) imaging, convergent beam electron diffraction (CBED), selected area diffraction (SAD), and energy dispersive spectroscopy (EDS). Quantitative EDS calculations were based on the Cliff–Lorimer approximation.[41] The camera length constant for the microscope was determined from a specimen of evaporated gold deposited on to holey carbon film. The diffraction patterns for gold and the various specimen images were collected digitally and distances were measured using a free-ware image analysis software package (*MacLispix*) made available by the National Institute of Standards and Testing (NIST).[42] Quantitative particle size measurements were made with the image analysis program *Object-Image*[43] using micrographs taken with a calibrated CCD camera (Gatan Multi-Scan camera, Gatan, Inc., Pleasanton, CA).

2.4. X-ray diffraction

Initial X-ray diffraction studies were conducted with a CuK_α source on a standard laboratory diffractometer, (Giegerfiex DMax automated powder diffractometer, Rigaku/USA, Danvers, MA) equipped with a graphite monochromator. The diffractometer was operated at a voltage of 40 kV and a current of 40 mA with a slit system of: 1/2–1/2°–0.3–0.8 mm. The data was collected in a theta–2-theta scanning mode. Spectra were collected from crushed, quenched beads, before and after crystallization in thermal analysis experiments. For crystallized specimens, typically a goniometer speed of 2° 2θ/min was used with a step size of 0.01° 2θ, and the data was summed over 10 scans. For quenched specimens, typically a goniometer speed of 2° 2θ/min was used with a step size of 0.01° 2θ, and the data was summed over 50 scans.

Detailed crystal structure measurements of annealed powder specimens (M1, M2, M3 and M4, Table 1) were made at the Advanced Photon Source (APS) at the Argonne National Laboratory at the UNICAT beamline E33 (the undulator). Specimens were chosen to represent various stages of mullite crystallization (Table 1). The beam cross section was approx. 2×1 mm and the wavelength was 0.75266 Å, as determined by Rietveld refinement of a Si standard (SRM 640b, National Institute of Standards). Specimens were loaded in a capillary tube with a 0.5 mm ID, which was rotated at a minimum rate of 60 rpm. The data was collected by step scanning a single slit scintillation counter, versus a constant monitor counting rate. Minimum counting times of about 1 s per step were chosen to achieve at least one revolution of the capillary sample spinner. An angular range of 5.0–37° 2θ (8.6276–1.1860 Å) was scanned at a step size of 0.008°, yielding 4000 data points per powder diagram.

3. Results and discussion

3.1. Thermal analysis

The Johnson–Mehls–Avrami (JMA) equation [Eq. (1)] was the basis for modeling non-isothermal DSC experiments. Although this equation was derived for isothermal phase transformations, it has been successfully applied to non-isothermal DTA or DSC experiments under appropriate experimental conditions.[44–48] The key relationship observed is the variation of the crystallization temperature, T_p, with heating rate, α. Since the crystallization exotherm is not a delta function, but rather a curve that occurs over a range of temperatures, it is important to determine the temperature at each heating rate that corresponds to the same degree of crystallization. This is necessary to accurately model the a α vs. T_p trend.

Table 1
The designation, thermal history and description of specimens characterized by various techniques

Symbol	Thermal history	Analyses	Form	Details
Q	Quenched glass	DSC, TEM, XRD	Powder, thin film	Glass beads received from CRI
N	10°C/min to 920°C, 3 h	DSC, TEM	Powder, fiber	Highest annealing temperature observed in DSC without crystallization exotherm
M1	40°C/min to 938°C, 2.5 h	DSC, TEM, synchrotron.	Powder	Pseudotetragonal mullite formed at a low temperature
M1.5	10°C/min to 1085°C, 0.5 h	TEM	Thin film	Polished thin film specimen of psuedotetragonal mullite
M2	10°C/min to 900–930°C, 3 h, various rates to 1200°C	TEM, XRD, synchrotron	Powder	Pseudotetragonal mullite prior to transition to orthorhombic phase. Mixture of powders
M3	10°C/min to 1400°C	TEM, synchrotron	Powder	Orthorhombic phase
M4	Kyoritsu KM101	XRD, synchrotron	Powder	Source material

It has been demonstrated that the maximum in the crystallization exotherm corresponds to approximately 55% conversion, independent of the heating rate.[45] Thus the temperature at the exothermic peak (T_p) was chosen as the reference temperature in these studies.

$$x = 1 - \exp[-(kt)^n] \quad (1)$$

A pre-requisite for using JMA based equations for kinetic analysis of non-isothermal experiments, as pointed out by Ray et al.,[47] is that the specimen must be thoroughly nucleated prior to crystal growth so that crystallization occurs with a constant number of nuclei. This precludes a situation where nucleation and growth occur simultaneously. Experimental conditions where crystallization occurs with a constant number of nuclei is also an important factor for using the equation for the reaction rate, k [Eq. (2)]. The reaction rate is typically assumed to have an Arrhenius temperature dependence, and to be independent of time. In order to minimize errors when calculating the reaction rate, non-isothermal crystallization experiments should be designed to occur within a narrow temperature range and with a near-zero nucleation rate.[47]

$$k = \nu \exp\left[\frac{-E}{RT}\right] \quad (2)$$

The kinetic model proposed by Bansal and Doremus[44,45] was used to analyze the non-isothermal crystallization data for these experiments. The final result of their derivation is shown in Eq. (3). A plot can then be made of $\ln(\alpha/{T_p}^2)$ vs. $1/T_p$. This type of plot is sometimes termed a Kissinger plot.[47,49]

$$\ln\left(\frac{{T_p}^2}{\alpha}\right) = \frac{E}{R}\left(\frac{1}{T_p}\right) + \ln\left(\frac{E}{R\nu}\right) \quad (3)$$

The slope of the line through the data points is used to calculate the activation energy for crystallization, E, and the y-intercept of the line is used to calculate the pre-exponential factor, ν in Eq. (2).

The other variable yet remaining to be calculated from the data is the Avrami exponent, n. The method of Augis and Bennet[50] was used, Eq. (4).

$$n = \frac{2.5}{\Delta T_{FWHM}}\left(\frac{{T_p}^2}{E/R}\right) \quad (4)$$

The value of the Avrami exponent provides information regarding the morphology of the growing crystals. For conditions where crystallization occurs throughout the bulk of the material with a constant number of nuclei, the value of n indicates the dimensionality of the growing crystals.[47] All of the pertinent variables (n, k, E and ν) for the JMA equation [Eq. (1)] were thus computed from the non-isothermal data.

3.1.1. Nucleation studies

Nucleation experiments were carried out to determine necessary annealing conditions to saturate the quenched glass with nuclei. Since the nucleation rate is a function of time and temperature similar to crystal growth,[51] there is a variation of T_p with the soak temperature, T_N. The soak temperature where T_p is the lowest, is where the nucleation rate is a maximum. Annealing the specimens at this temperature would thus saturate them with nuclei and establish appropriate conditions for non-isothermal crystallization studies. This variation is typically pronounced for strong, glass-forming systems, (e.g. Li_2O–Al_2O_3–SiO_2 glasses).[47,48]

Nucleation rate studies on quenched mullite composition glass beads did not show a significant variation of T_p with T_N. The standard for comparison was a specimen heated at a rate of 10.0°C/min from room temperature to 1100°C. There was no significant difference in T_p between the standard sample heated at 10.0°C/min and those subjected to the various annealing treatments. The specimens isothermally held at 930 and 940°C crystallized during the hold time. The results are listed in Table 2. Thus, it was concluded that the specimens were fully nucleated by the time they reached 850°C, and that further annealing treatments were unnecessary. These findings seemed reasonable, since mullite is a very fragile glass forming material.

3.1.2. Crystallization kinetics

Non-isothermal DSC crystallization experiments with quenched mullite composition specimens were conducted as previously stated. Results for the heating rate, T_p, and the Avrami exponent, n, are listed in Table 3. A Kissinger type plot[49] [Fig. 1, based on Eq. (3)] was used to calculate the activation energy, E, and pre-exponential factor, ν.

A significant change in slope between 3.0 and 4.0°C/min heating rates was observed in Fig. 1. This indicated that more than one kinetic mechanism was involved in the crystallization process. A closer examination of the DSC exotherms at these lower heating rates (e.g. <6°C/min) revealed that there were two different exothermic

Table 2
Variation of crystallization temperature, T_p, with annealing temperature, T_N, for crystallization of quenched mullite composition glass beads

Nucleation temperature T_N	Crystallization temperature, Tp
10°C/min Ramp	984.6°C
850°C/3 h	985.5°C
890°C/3 h	984.6°C
900°C/3 h	986.0°C
910°C/3 h	985.9°C
920°C/3 h	987.2°C
930°C/3 h	–
940°C/3 h	–

Table 3
Kinetic data for the crystallization of quenched mullite composition beads from non-isothermal DSC studies

α (°C/min)	T_p (°C)	n
0.5	945.7	3.56
1.0	955.5	3.50
1.5	959.4	3.37
2.0	965.0	3.16
3.0	970.5	3.29
4.0	977.1	2.69
5.0	979.4	3.47
6.0	980.3	2.82
8.0	983.4	6.91
10.0	986.1	16.7
E_1 (kJ/mol)	892	
E_2 (kJ/mol)	1333	
ν_1 (s^{-1})	$1.02E+35$	
ν_2 (s^{-1})	$3.56E+53$	
n[a]	3.23 ± 0.3	

[a] Average value, not including 8.0 and 10.0°C/min.

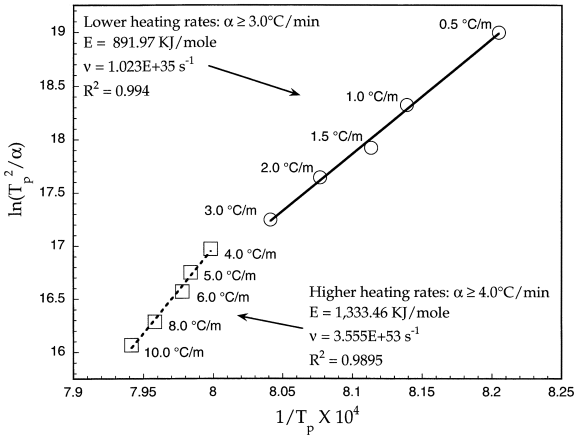

Fig. 1. Kissinger plot $\left(\ln\left(T_p^2/\alpha\right)\right.$ vs. $\left.1/T_p\right)$ for non-isothermal crystallization of quenched mullite beads. Note that there were two different crystallization regimes, with a break between heating rates of 3.0 and 4.0°C/min.

events that occurred during crystallization. At heating rates $\leqslant$3.0°C/min, the first event was dominant, whereas at heating rates $\geqslant$4.0°C/min, the second event became dominant. Fig. 2 is a comparison of the DSC exotherms at 3.0 and 4.0°C/min, showing the two different exothermic events, and the shift in dominance between them. The values for T_p listed in Table 3 were the more prominent of the two. At heating rates above 5.0°C/min, the two peaks overlapped sufficiently so that it was very difficult to differentiate between them. For $\alpha\geqslant$8.0°C/min, the increased intensity and overlap of the two events created significant asymmetry in the shape of the crystallization exotherms.

The coefficient of determination (R^2) for the line fit applied to heating rates $\leqslant$3.0°C/min on Fig. 1 was

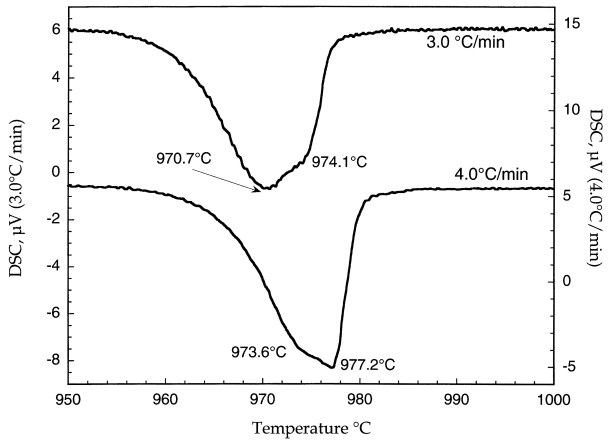

Fig. 2. Plot of the DSC exotherms for non-isothermal crystallization of quenched mullite composition glass, at heating rates of 3.0 and 4.0°C/min. Note the asymmetry in both curves, indicating two different exothermic events, as well as the shift in prominence between the two different events from 3.0 to 4.0°C/min.

0.994 and the value of R^2 for the line fit applied to heating rates $\geqslant$4.0°C/min was 0.9895. The activation energies for crystallization were 892 and 1333 kJ/mol for the first and second events, respectively. The values of the Avrami exponent, n, in Table 3 were calculated based on Eq. (4). The combined average value of n, was 3.23 ± 0.3, which indicated three dimensional crystal growth. (The values of n for $\alpha = 8.0$ and 10.0°C/min were not included in the average due to the significant asymmetry in the shape of the crystallization exotherm.) The values for ν ($1.02E+35$ s^{-1}, and $3.56E+53$ s^{-1} for events one and two, respectively) were rather large. Since mullite is a fragile glass former, and these values were determined from the extrapolated value of the y-intercept from Fig. 1 using Eq. (3), there may be somewhat of a large margin of error in the computed values of ν. Nonetheless, they do reflect the rapidity at which amorphous mullite composition glasses crystallize.

The activation energy for mullite crystallization has been reported to be precursor dependent.[23] Nonetheless, the calculated activation energies for mullite crystallization in this system lie within the range of values reported in the literature, e.g. ~850–1300 kJ/mol.[20,22,23,52,53] Additionally, a similar phenomena of two over-lapping crystallization exotherms for mullite crystallization was reported by Tkalcec et al.[20] who characterized the crystallization kinetics of single-phase, solgel derived, mullite precursors using isothermal DSC experiments. Takei et al.[53] reported a three-stage crystallization sequence in alumino-silicate fibers. The two mullite crystallization activation energies reported here, (892 kJ/mol and 1333 kJ/mol) correlate very well with the two activation energies for the first stage of mullite crystallization for a 49 mass% Al_2O_3 fiber reported by Takei et al.[53] (E_a^N for nucleation was 864 kJ/mol and E_a^{NG} for nucleation and growth was 1288 kJ/mol). Their

three stage crystallization sequence (Stage 1 = 900–1000°C, Stage 2 = 1000–1200°C and Stage 3 = 1200–l400°C) was determined by quantitative XRD analysis of amorphous alumino-silicate fibers crystallized after various thermal treatments. Thus, it was significant to note that the non-isothermal DSC derived kinetic data reported here, for the crystallization of quenched mullite composition glass (at temperatures below 1000°C), was similar to that determined by Takei et al.[53] for their stage one (900–1000°C) crystallization of amorphous alumino-silicate fibers using quantitative XRD analysis.

The two different exothermic events observed during crystallization were probably the result of two slightly different composition mullite phases crystallizing. The two different composition mullite phases were most likely the result of phase separation that occurred in the mullite composition beads during quenching and cooling of the beads. TEM analysis of as-received, quenched, mullite composition beads (discussed in the next section) shows evidence of this. As with all glass systems, the quench and cooling history of the specimen affects its microstructure, and subsequent devitrification behavior. Additional phase separation was also probable when the specimens were heated up to their crystallization temperature during thermal analysis experiments.[54] This was similar to the thermal processing that Tkalcec et al.[20] applied to the sol-gel precursors they examined, where multiple crystallization events were also observed (using isothermal DSC experiments). The thermodynamic basis for phase separation in the Al_2O_3·SiO_2 phase diagram is the existence of a metastable immiscibility gap, which has been reported by several other investigators.[54–58] In fact, Huling and Messing[59] reported that all quenched aluminosilicate glasses are phase separated, and that phase separation proceeds more rapidly than crystallization for amorphous mullite composition gels and glasses. The shift in the prominence of the two exothermic events indicates the possibility of competing crystallization mechanisms between the two compositions. Microstructural characterization and Rietveld analysis were conducted to corroborate the existence of multiple phases in mullite crystallized at low temperatures. Those findings are discussed below.

3.2. Microstructure

3.2.1. As-received and nucleated specimens (Q and N)

Specimens Q and N (Table 1) were used to characterize the as-received mullite beads, and to examine the microstructure of mullite just prior to crystallization. Fig. 3 is a TEM bright field (BF) (A) and a STEM BF (B) micrograph of a polished, thin section from an as-received, quenched mullite bead (specimen Q). The contrast observed in the specimen was typical of phase-separated, amorphous materials. Even though the starting composition of the specimen was $3Al_2O_3$·$2SiO_2$, chemical analysis at various points revealed significant variations in composition. For example, the chemical composition for the field of view in Fig. 3B was 75.8 mol% Al_2O_3 and 24.2 mol% SiO_2. Additionally, there was a wide variation in the Al/Si ratio within the field of view in Fig. 3B. The variation in the Al/Si K_α ratio within Fig. 3B is shown by an EDS line scan superimposed on the micrograph. Based on the Cliff–Lorimer approximation,

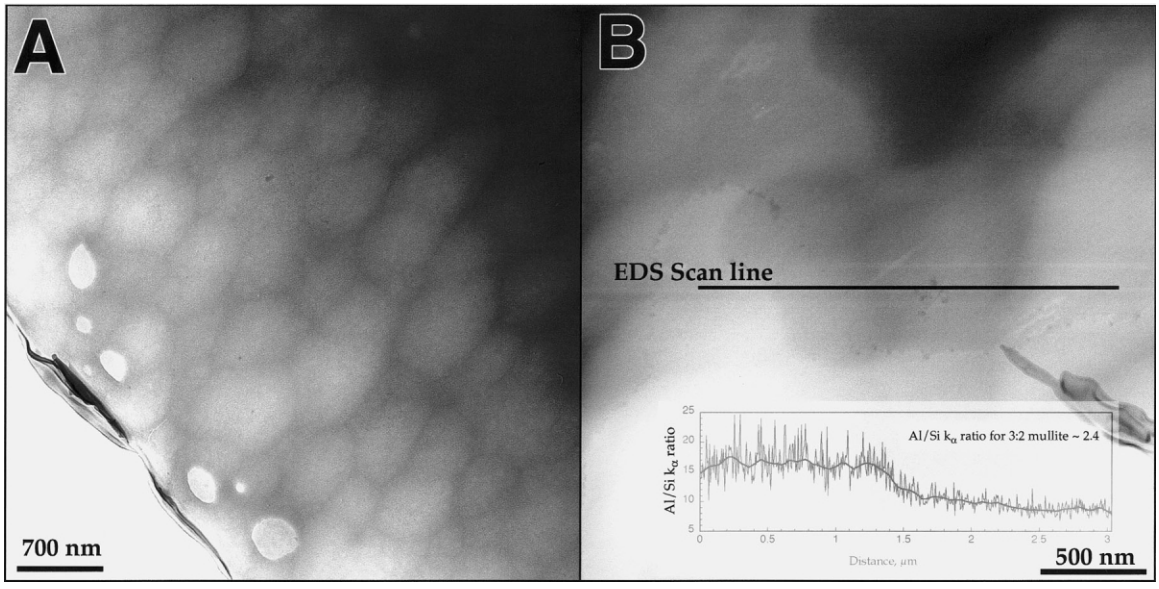

Fig. 3. TEM BF image (A) and STEM BF image (B) of a polished thin section from an as-received, quenched, mullite composition bead (specimen Q). The contrast variations in (A) were typical of phase-separated, amorphous materials. The entire field of view in (B) had a composition of 75.8 mol% Al_2O_3 and 24.2 mol% SiO_2, as determined by STEM EDS. The graph in (B) shows the variation in the Al/Si K_α ratio from an EDS line scan through the central dark region in the sample. An Al/Si K_α ratio of 2.4 corresponds to 3:2 mullite (60 mol% alumina).

the ratio of the intensities of the K_α peaks is proportional to the ratio of the concentrations (in wt.%, for this data).[41] For an assumed theoretical proportionality or sensitivity factor (k_{AlSi}) of 1.2,[41] an Al/Si K_α ratio of ~2.4 would indicate an Al/Si wt.% ratio of 2.89:1, (molar ratio of 3:1), which would correspond to $3Al_2O_3{\cdot}2SiO_2$ mullite. Even though the counting statistics for the EDS line scans were not sufficient for quantitative analysis, the data demonstrated that the specimen was inhomogeneous; the average Al/Si K_α ratio varied from approx. 16–8 over a distance of 3 μm. The observed chemical inhomogeneity for the quenched specimens was consistent with reports of a metastable immiscibility gap in the Al_2O_3–SiO_2 phase diagram.[55–58] This apparent phase separation may have been responsible for the two crystallization events observed by DSC.

Fig. 4 is a TEM BF micrograph of a quenched, amorphous, melt-drawn mullite fiber that was annealed at 920°C for 3 h (specimen N, Table 1). This thermal treatment was the highest annealing temperature that was observed in the DSC, without the onset of complete crystallization (Table 2). The dark regions were examined by selected area diffraction (SAD), and were identified as small crystallites. The SAD pattern of the crystallites is shown in the inset image in Fig. 4A. The pattern was indexed as belonging to the pseudotetragonal metric of mullite. The sizes of 150 crystallites were measured, and the average lengths of the major and minor axes were 13.4±2.9 and 11.5±2.7 nm, respectively (Table 4). A high resolution micrograph of one of the crystallites is shown in Fig. 4B. The d-spacing for the lattice fringes in this crystallite was 3.38 Å, which is close the d-spacing for the (120) and (210) lattice planes of orthorhombic mullite (3.428 and 3.390 Å, respectively). It was only possible to resolve one ring near this d-spacing in the SAD pattern, which is consistent with psuedotetragonal mullite.

3.2.2. Pseudotetragonal mullite (M1, M1.5 and M2). The thermal treatments applied to specimens M1 and M2 were chosen in order to characterize pseudotetragonal mullite after initial formation and just prior to conversion into orthorhombic mullite,[10,17,19] These specimens correspond to the first and second crystallization stages reported by Takei et al.[53] Specimen M1.5 was used to compare the effects of sample preparation (powders vs. thin film) on microstructure for pseudotetragonal mullite and to examine the microstructure at an intermediate temperature. Fig. 5 is a TEM BF micrograph of a crushed, quenched, mullite composition bead that was crystallized isothermally by annealing it at 938°C for 2.5 h (specimen M1). The microstructure consisted of a matrix of angular, crystalline grains (~370×260 nm in size) with smaller, ellipsoidal inclusions (average size = 10.0×7.8 nm) embedded in them (Table 4). Fig. 6 is a pair of BF (A) and DF (B) micrographs at higher magnification of another particle from the same specimen. The right portion of Fig. 6A was one of the grains; the smaller, rounded, lighter features were the inclusions. In bright field mode, the grains had a variegated diffraction contrast (Fig. 5), where different regions of the grain would go in and out of extinction in a sweeping fashion as it was tilted. Fig. 6B is the same area as Fig. 6A, only in a dark field condition. The beam was tilted so that a particular set of lattice planes from the grain were allowed to pass through the objective aperture, thus

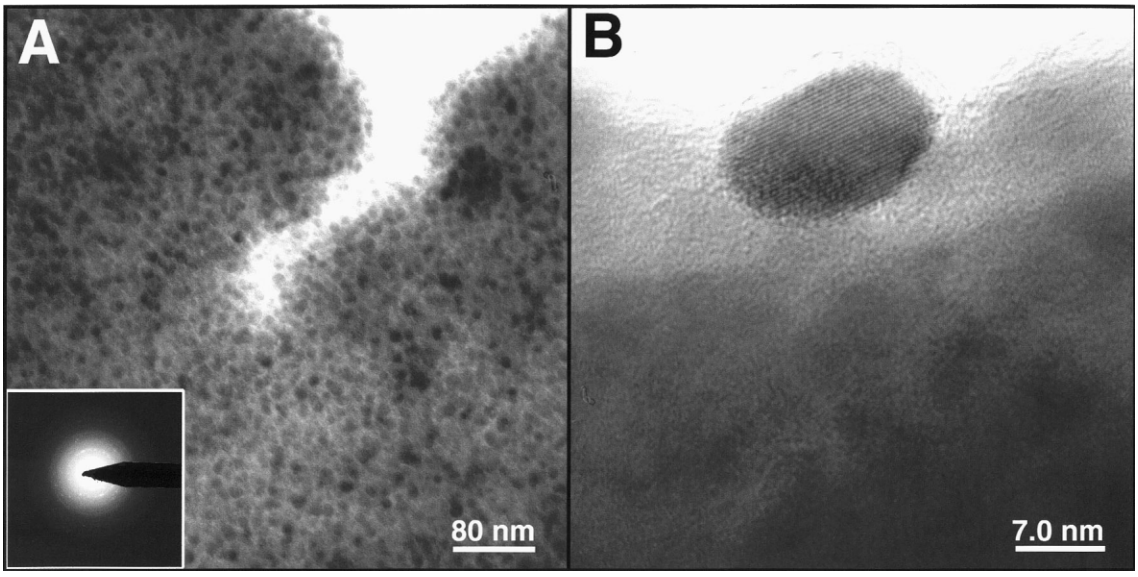

Fig. 4. TEM BF images of an amorphous mullite fiber annealed at 920°C for 3 h (specimen N). The inset image in (A) is an SAD pattern taken from the crystallites along the edge. The pattern was indexed as the pseudotetragonal metric of mullite. The lattice spacing of the crystallite in (B) was 3.38 Å, which corresponded to the (l20)/(210) lattice planes of mullite (3.428 and 3.390 Å, respectively).

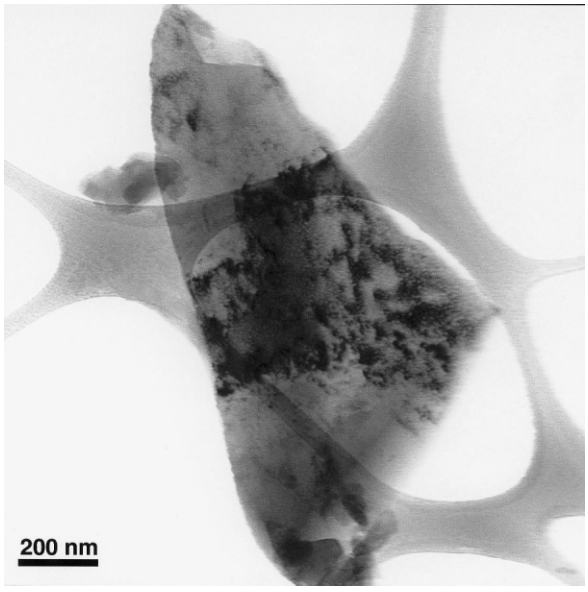

Fig. 5. TEM BF micrograph of a crushed, quenched, mullite composition bead that was isothermally crystallized at 938°C for 2.5 h (specimen M1).

creating the bright band in Fig. 6B. The dark circular features were the ellipsoidal inclusions.

Fig. 7 consists of two TEM BF micrographs from a polished thin section of a quenched mullite bead that was heated to 1085°C for 0.5 h (specimen M1.5). EDS analyses were taken at the ten different labeled points in Fig. 7A (beam diameter ~70–100 nm), and the average composition at each point was 60±1 mol% Al_2O_3, 40±1 mol% SiO_2. Fig. 7B is a micrograph from M1.5 at higher magnification centered around a single grain, where a large number of small, ellipsoidal inclusions embedded in the grain were also visible (similar to what was observed in Fig. 6). The inclusions appear as bright spots on the right side of the micrograph, and as dark spots on the left side. When the specimen was observed in over- and under-focused conditions at higher magnification (at the same angle of tilt), the contrast of the inclusions changed from dark areas with a light fringe to light areas with a dark fringe. This was interpreted as a Fresnel fringe effect due to a density difference between the inclusions and the matrix (inclusion density <matrix density).[41] The inset image is a [001] zone axis

Table 4
Particle size measurements for quenched mullite composition specimens after various thermal treatments

Specimen	Major axis (nm)	Minor axis (nm)	Average diameter (nm)	Average area (nm^2)	No. of measurements
N (crystallites)	13.4±2.9	11.5±2.7	12.6±7.9	123.8±49.3	150
M1 (inclusions)	10.0±2.2	7.8±1.9	9.0±5.6	63.0±24.8	150
M1 (grains)[a]	~370	~260	~350	9.6E+04	40
M1.5 (inclusions)	9.4±2.5	7.9±2	8.8±6.4	61.4±32	150
M1.5 (grains)[a]	~510	~380	~510	2.03E+05	50
M2 (inclusions)	7.9±1.7	6.6±1.5	7.3±4.7	42.2±17.43	150
M2 (grains)[a]	~270	~190	~257	5.2E+04	135
M3 (grains)	100±55	69±38	~99	7.68E+03	60

[a] Broad size distribution.

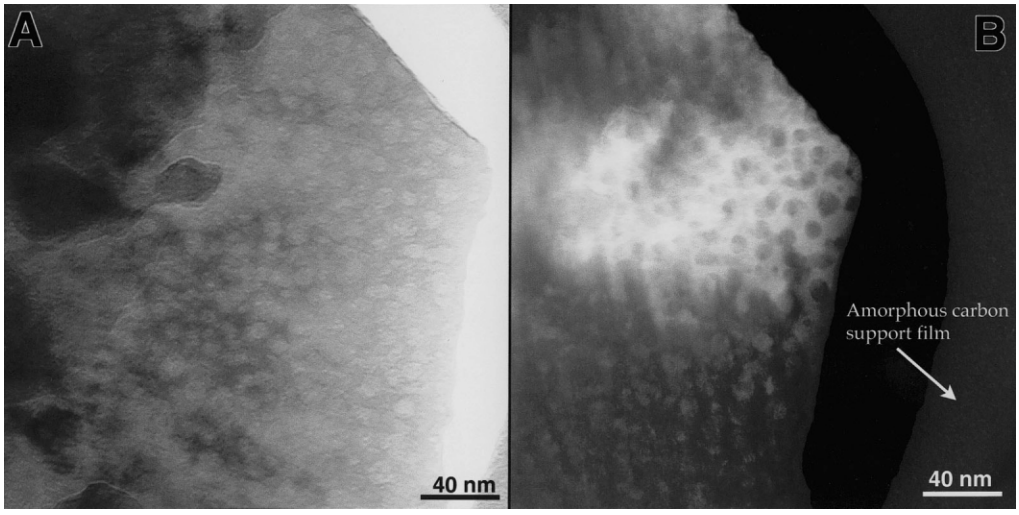

Fig. 6. TEM BF (A) and DF (B) micrographs of a ground sample from a quenched mullite composition bead that was isothermally crystallized in a DSC at 938°C for 2.5 h (specimen M1). The darker, matrix region in the BF image (A) appeared as the bright region in the DF image (B), and the light, circular inclusions observed in the BF image appeared dark in the DF image.

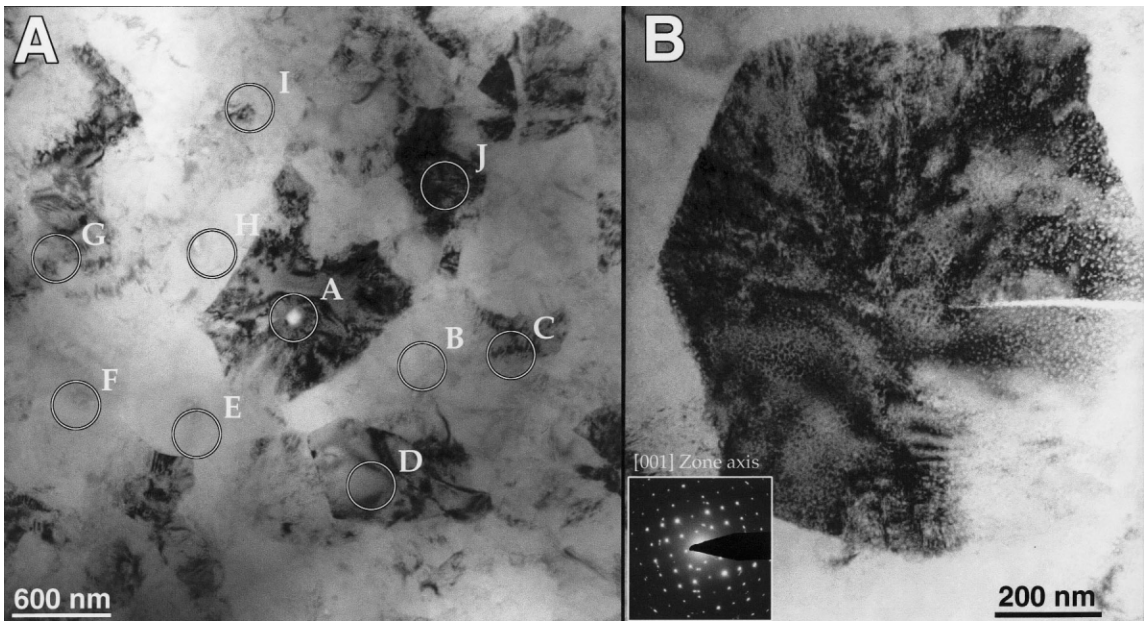

Fig. 7. TEM BF images (A and B) from a polished thin section of a quenched mullite composition bead that was heated to 1085°C (M1.5). EDS analyses were made at the points labeled alphabetically, and the composition at each point was 60±1 mol% Al_2O_3, 40±1 mol% SiO_2. The variegated contrast in the grains was due to internal strain. Higher magnification of one of the grains (B) revealed small inclusions with and average size of 9.4×7.9 nm. The SAD pattern in (B) was taken from the [001] zone axis of a similar grain.

SAD pattern taken from another grain in this specimen. Any extra spots in the pattern not belonging to the zone axis were identified to originate from an adjacent or overlapping grain by DF mode, and were not from the inclusions. Qualitatively, the microstructures for M1 and M1.5 appeared very similar, however, quantitatively, subtle differences were noted. For M1.5, the average lengths of the major and minor axes for 150 small, ellipsoidal, inclusions were 9.4±2.5 and 7.9±2 nm, respectively, and the average sizes of the major and minor axes for the grains were ~510 and 380 nm, respectively (Table 4).

Fig. 8 is a STEM BF micrograph of specimen M1.5. The composition over an area of about 10 μm^2 was 58 mol% Al_2O_3 and 42 mol% SiO_2, as measured by this EDS detector. However, when spot analyses (probe diameter ~15 nm) were done at specific points, compositions as low as 42 mol% Al_2O_3 and 58 mol% SiO_2 were found. The higher silica content determined by spot analysis was thought to be due to the smaller diameter beam being centered on areas with a high density of inclusions (beam diameter ~15 nm, inclusion diameter ~9 nm). If the composition of the inclusions were higher in silica than the crystal matrix, a region with a high density of inclusions would affect the EDS results. Rigorous, quantitative analysis however, was complicated by beam damage to the specimen. The inset graph in Fig 8 is an EDS line scan that illustrates the variation in the Al/Si K_α ratio over a distance of approx. 200 nm. Several different peaks and valleys were observed between Al/Si K_α ratios of 1:1 to 3:1. The important feature of this data, was that the smaller diameter beam was able to reveal chemical heterogeneity in this specimen on a sub-micron scale. This was in contrast to the EDS data collected for the same specimen in Fig. 7A, where the EDS analysis was done on a TEM using a much larger diameter beam (~70–100 nm).

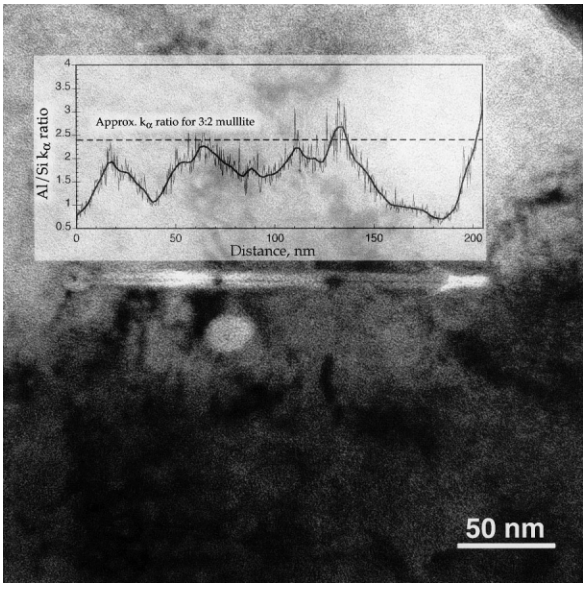

Fig. 8. STEM BF micrograph of a quenched mullite bead heated to 1085°C (M1.5). The horizontal line in the center of the micrograph was due to beam damage of the specimen during EDS line profile analysis. The inset graph shows the variation in the Al/Si K_α ratio over the region scanned. This was an indication of chemical inhomogeneity at very small length scales.

Fig. 9 is a TEM BF micrograph of a crushed, quenched mullite composition bead that was heated to 1200°C (specimen M2). The inset image is a Kossel-Möllenstedt (KM) microdiffraction pattern taken from one of the crystals oriented along the [120] zone axis for mullite. The average grain size was 270×190 nm. Small inclusions embedded within the grains were also observed, with an average size of 7.9±1.7×6.6±1.5 nm (Table 4). The variegated diffraction contrast observed in specimens M1 and M1.5 was still present. EDS analysis conducted at several different locations on several different particles indicated a nominal composition of 60± 2 mol% Al_2O_3, and 40±2 mol% SiO_2.

3.2.3. Orthorhombic mullite (M3). Fig. 10 is a TEM BF micrograph of a crushed, quenched mullite composition bead that was heated to 1400°C (M3). This thermal treatment was chosen in order to characterize the microstructure of mullite after conversion to the orthorhombic phase, and prior to the temperature where it begins to exsolve SiO_2.[2,3] This thermal treatment also corresponds to the end of stage 3 crystallization reported by Takei et al.[53] The average grain size was 100×69 nm. A typical, polycrystalline microstructure was observed. The variegated diffraction contrast, and the small inclusions observed at lower temperatures were almost completely eliminated.

3.2.4. Microstructural observations. The microstructure and EDS analysis of as-received, quenched, mullite composition beads (Fig. 3) demonstrated that these specimens were phase separated. This was consistent with other reports in the literature for quenched aluminosilicate glasses.[55,56,59] As stated previously, phase separation is common in even the most rapidly quenched aluminosilicate glasses.[59] Consequently, phase separation was probably responsible for the two crystallization events characterized by non-isothermal DSC analysis.

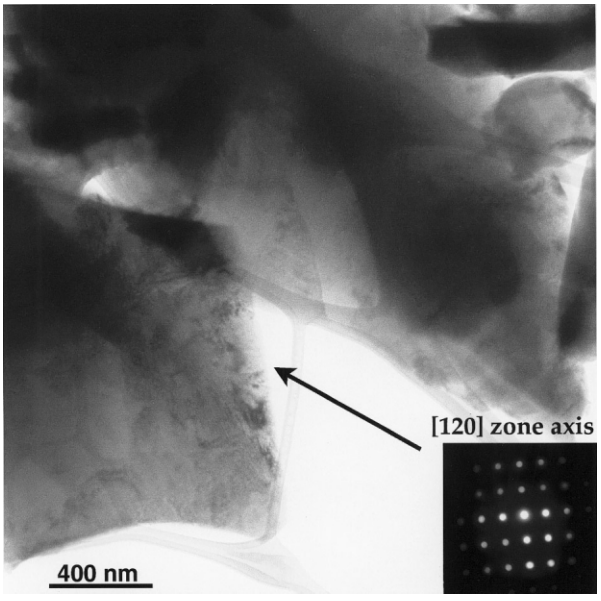

Fig. 9. TEM bright field image of a quenched mullite composition powder after being heated up to 1200°C (specimen M2). The inset image is a Kossel–Möllenstedt microdiffraction pattern for the designated crystal oriented along the [120] zone axis.

The presence of discrete crystallites observed at the very early stages of crystallization (Fig. 4) was evidence that crystallization proceeded via a nucleation and growth mechanism. The large number of crystallites uniformly dispersed throughout the specimen indicates that the material was site saturated, that crystallization occurred with a constant number of nuclei, and that crystallization occurred throughout the bulk of the material (vs. just at the surface). These observations were consistent with the results from the DSC nucleation experiments.

There were several common features to the microstructures of specimens M1, M1.5 and M2. Although there was a large distribution in grain sizes, they all had fairly equiaxed grains (Figs. 5 and 7). The grains showed a variegated diffraction contrast, that in several of the micrographs appeared to originate from the center of the grain (Fig. 7). This suggests that crystallization occurred three dimensionally, and that the crystals grew spherulitically, from a point of origin. Three dimensional crystal growth occurring throughout the bulk of the material is characteristic of an Avrami exponent equal to three. The computed value of n from DSC experiments was 3.23. Thus, the observed microstructure was consistent with the kinetic parameters determined by non-isothermal DSC experiments.

The microstructure for these specimens was similar to reports in the literature for other pseudotetragonal mullite specimens. MacDowell and Beall[55] used the term "rosette" to describe the morphology they observed. Their description was similar to the spherulitic grain growth reported here. Huling and Messing[59] also used the term "rosette" to describe the grain morphology of their specimens. Additionally, they reported that for their sol-gel derived mullite precursors crystallized at 1000°C for 2 h, the alumina-rich, pseudotetragonal mullite grains had impinged throughout the gel. They also stated that the silica-rich phase remained amorphous and was enveloped by the metastable pseudotetragonal mullite. This appears to be similar to the embedded inclusions reported here.

The variegated diffraction contrast in M1, M1.5 and M2 was an indication that the crystal lattice of these specimens was distorted, possibly by internal strain (strain originating from within the crystal, such as caused by interstitial or substitutional dopant atoms slightly larger than a given site). That is, for each individual single crystal grain, regions of atoms were displaced from their normal, ideal, equilibrium position. Conceptually, if a

flat piece of paper were used to represent a perfect plane of atoms in a perfect crystal, then a wrinkled piece of paper would represent a plane of atoms that was distorted by internal strain. A distorted lattice will cause an incident electron beam to diffract in a wavy manner, as observed in Figs. 5–9.[41] Although several of the TEM specimens were made from ground powders, the observed strain probably was not an artifact of sample preparation. Specimen M1.5 (Figs. 7 and 8) was prepared as a thin foil by tripod polishing and ion milling, and it had the same variegated diffraction contrast as the ground powder specimens M1 and M2 (Figs. 5, 6 and 9). Specimen M3 (orthorhombic phase, heated to 1400°C, Fig. 10) was another crushed powder specimen, however, it contained very few grains with variegated diffraction contrast, most of them appeared strain free, and exhibited typical contrast changes when tilted in BF mode. Additionally, the specimens were ground while amorphous, and examined after crystallization. The high temperatures and structural rearrangement that occurred during crystallization should have been sufficient to relieve any residual strain induced in the material from grinding.[60] These observations suggest that the observed microstructure for the pseudotetragonal mullite specimens was not an artifact of sample preparation, but that these specimens naturally had a very strained or distorted crystal lattice, and that the source of lattice distortion was internal to the crystal, and not externally imposed (Fig. 7).

The other feature common to specimens M1, M1.5 and M2 was that they all contained numerous inclusions, ~7– 10 nm in size. The exact chemical composition and structure of these inclusions was not conclusively determined. Several different microscopes (LaB_6 TEM, FEG STEM, and FEG TEM) and microscopic techniques were used to examine them microstructurally and microchemically, including EDS, SAD, convergent beam electron diffraction (CBED), electron energy loss spectroscopy (EELS), and elemental mapping with an energy filtered TEM. Their small size necessitated a very small diameter electron beam to probe them individually, however the specimens were susceptible to beam damage, making them difficult to analyze. Since they were very similar chemically to the crystal matrix that they were embedded in, it was difficult to differentiate their chemical identity using broader diameter electron beam analyses (e.g. energy filtered elemental mapping). High resolution TEM analysis of the interface between the matrix and the inclusions was also complicated by beam damage.

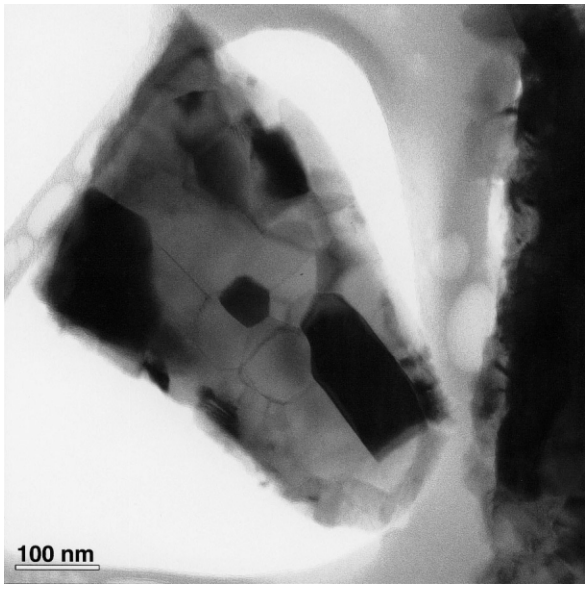

Fig. 10. TEM bright field image of quenched mullite composition powder after being heated up to 1400°C (specimen M3).

However, zone axis SAD patterns were obtained from grains containing the inclusions (Fig. 7B). If the inclusions were crystalline, and randomly oriented within the matrix crystal, it would be plausible to see a SAD pattern containing both the zone axis pattern for the matrix crystal along with a ring pattern from the numerous inclusions. Or, if the inclusions were crystalline, and epitaxially related to the matrix, then extra reflections might appear in zone axis SAD patterns. However, neither of these phenomena were observed. Any additional reflections in the SAD pattern that did not belong to the zone axis were identified (by DF) to belong to either a different region from the strained grain (in a different diffracting condition), or from a adjacent or overlapping grain. This evidence would indicate that the inclusions were amorphous.

Additional evidence concerning the identity and structure of the inclusions can be inferred from other experiments. Rietveld analysis of specimens M1 and M2 (discussed later) revealed that the crystals were alumina rich (~70 mol% Al_2O_3) based on their lattice parameters, and their XRD spectra showed a broad amorphous hump centered around the 100% peak as well as at higher angles. TEM EDS analysis with a moderate diameter electron beam (70–100 nm) on specimens M1.5 (Fig. 7A) and M2 indicated a composition close to 60 mol% Al_2O_3, whereas STEM EDS analysis using a much smaller probe diameter ($\leqslant$15 nm) showed significant compositional variations over a smaller length scale (Fig. 8). The correlation of this information indicated the existence of an amorphous, SiO_2-rich phase that was very small and dispersed on a very fine level. It would appear that the inclusions observed in specimens M1, M1.5 and M2 were this phase. Huling and Messing[59] also reported a silica-rich phase present in, and enveloped by, metastable pseudotetragonal mullite.

These inclusions may have been the cause of strain or lattice distortions observed in specimens M1, M1.5 and M2. Since the silica-rich inclusions were embedded within the crystal grains (vs. collecting along grain

boundaries), the crystal lattice had to form around them, or accommodate them within the structure. Consequently, the crystal lattice appears to have been distorted by their presence. Referring back to the previous analogy of crystal planes and sheets of paper, a perfect crystal could be thought of as a stack of perfectly flat sheets of paper, whereas the embedded, silica-rich inclusions could be thought of as a large number of small marbles interspersed between the sheets of paper (crystal planes). The polycrystalline microstructure was then an interlocking arrangement of different stacks of paper, each with their own orientation, and each embedded with a large number of small marbles.

TEM BF and DF analysis was used to show the spatial correlation between the lattice distortions and the inclusions. The analysis was done on two overlapping grains in specimen M1. For the centered DF (CDF) micrograph, the beam was shifted such that two closely spaced reflections (one from each grain) were allowed to pass through the objective aperture (inset, Fig. 11A). This set up a condition where a moiré pattern was formed by the overlapping lattice planes for the two grains.[41] This was seen in the CDF micrograph by thin, dark wavy lines passing through region where the grains overlapped (Fig. 11A). The moiré pattern was revealed in greater detail by (i) taking the Fourier transform (FFT) of the CDF image (inset, Fig. 11B), (ii) applying a filter to the FFT to remove everything except the periodic features, and then (iii) by taking the inverse Fourier transform of the filtered FFT. The filtered image is shown in Fig. 11B. The average spacing between the fringes was 8.56 Å, which was larger than any of lattice parameters for mullite. The regular periodicity of the lines, their presence throughout the region of overlap between the two grains, and the large spacing between them were all evidence that they were moiré fringes created by the overlap of lattice planes from two single crystals. This was confirmed by indexing the two reflections used to create the pattern, measuring their d-spacing, and the angle between them. The two spots were indexed as the (220) and (230) planes of mullite, their d-spacing was $d_{220} = 2.704$ Å, $d_{230} = 2.124$ Å (using the Rietveld refined lattice parameters for this specimen) and the angle between them was 7.85°. The calculated d-spacing for a general misfit moiré pattern, using the above values, was 8.62 Å.[41] This compared favorably to the measured fringe spacing of 8.56 Å, thus confirming the identity of the moiré pattern.

One of the important observations from the moiré pattern in Fig. 11B was that it was very distorted (wavy lines, dislocations, etc.), and the distortions were spatially correlated to the bright spots in Fig. 11A. The distortion in the moiré pattern was an indication that the crystal lattices were strained. The bright spots in Fig. 11A were the small, embedded inclusions from the second, or lower crystal that formed the moiré pattern. A cartoon in Fig. 11B illustrates how the image was formed. Thus, the conclusion drawn from Fig. 11 is that the inclusions created the distortion in the psuedotetragonal mullite lattice. The overlapping effects of the strain fields created by the numerous inclusions was consequently responsible for the complicated, variegated diffraction contrast observed in bright field micrographs of these specimens.

Table 4 lists the stereological measurements made on several of the specimens. The initial crystallites (~13.4×11.5 nm ellipsoids) apparently coalesced to

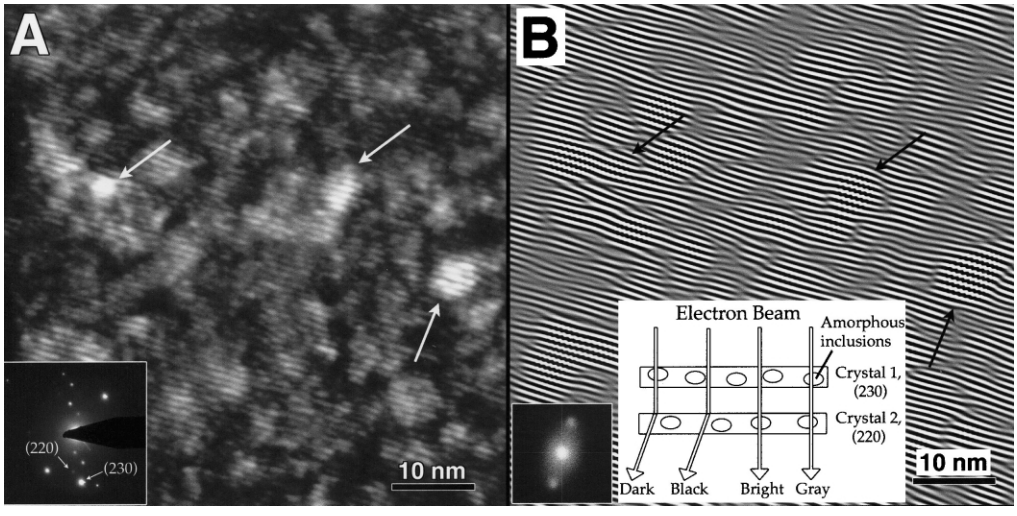

Fig. 11. TEM CDF micrograph (A) and corresponding moiré pattern (B) from pseudotetragonal mullite crystallized at 938°C for 2.5 h (M1). The micrograph was taken from an area of two overlapping crystals using the (220) reflection from one and the (230) reflection from the other (SAD inset, A). The overlapping lattice fringes from the two crystals created the moiré pattern (dark wavy lines). The cartoon in B explains the contrast observed in A. B is a filtered Fourier image of A showing the moiré pattern in greater detail. The inset in B was the fast Fourier transform (FFT) of A. The average fringe spacing in B was 8.56 Å; the computed fringe spacing from the SAD pattern was 8.62 Å. The distortion in the moiré pattern was an indication of strain in the two crystals, and was spatially correlated to the embedded inclusions in A (bright areas).

form larger, angular grains ~200×300 nm. The average grain size for M1.5 was significantly larger than for M1 and M2. This can be explained by the fact that it was crystallized as a monolithic disk bq~13 mm in diameter, and not as a powder like specimen M1 and M2. Additionally, since the specimen was made by polishing and thinning, it was possible to measure grains over a very large electron transparent region, whereas only selected thin areas from small particles could be measured for specimens M1 and M2. The grain size for specimen M2 was approx. 190×270 nm, which was about 27% smaller than M1.

Quantitative XRD studies of mullite crystallization showed a steady increase in crystallinity and volume fraction of mullite produced with increasing thermal treatment between 1000 and 1400°C.[8,14,53] Typically, an increase in crystallinity is accompanied by an increase in grain size, especially with increasing temperatures. However, in addition to a 27% reduction in grain size from M1 to M2, there was also a significant reduction in the size of the inclusions. From M1 to M1.5, there was a 6% reduction in the size of the inclusions, from M1.5 to M2 a 15% reduction, and from M1 to M2 a 22% reduction in the size of the inclusions. This indicates that with increasing temperature, the inclusions were gradually assimilated into the crystal, and that the average crystal size was decreasing. This finding was consistent with the interpretation that they were an amorphous, SiO_2-rich phase, since the SiO_2 content of psuedotetragonal mullite has been reported to increase (i.e. decreasing Al_2O_3 concentration) with thermal treatment.[3,10,14] The reported increased volume fraction of mullite crystallized over this temperature range from quantitative XRD studies thus appears to be related to the assimilation of these inclusions into the crystal. This may be microstructural evidence that the pseudotetragonal to orthorhombic transition, during the second crystallization stage of mullite, is diffusion limited, as reported by Li and Thompson[61] and Takei et al.[53] Apparently, concomitant with the assimilation of the SiO_2-rich inclusions, the large, spherulitic grains that initially form at low temperatures (Fig. 7) start to segment, or partition themselves into smaller grains, as the temperature increases during the second stage of mullite crystallization.

Specimen M3 contained a mixture of grains. Most of them did not contain inclusions, and did not display the variegated contrast observed in M1, M1.5 and M2. Those grains that did contain inclusions, however, contained a much lower density of inclusions than was observed in the pseudotetragonal mullite specimens, and they also appeared less strained. Of particular note was the ~67% reduction in grain size from M2 (1200°C) to M3 (1400°C). This was unexpected since grain size normally increases as a function of temperature. The reduction in grain size was most notable in those areas where there was a mixture of normal grains, and grains with inclusions. Typically in those areas, there was a large number of very small, normal, inclusion-free and strain-free grains around the perimeter of a strained grain that contained inclusions. It appears that the creation of new, smaller grains was a mechanism used to relieve the internal strain in pseudotetragonal mullite as is transitioned into orthorhombic mullite. A similar phenomenon has been observed in metallic systems, where highly strained metals recrystallize to form smaller grains after being annealed at elevated temperatures.[60] In addition to the inclusions, another source of strain in pseudotetragonal mullite is the anisotropic change in lattice parameter dimensions for the pseudotetragonal to orthorhombic transition (−0.93% for a, +0.23% for b, and −0.18% for c, discussed later).

3.3. XRD

X-ray diffraction measurements of crushed, quenched mullite composition beads were made before and after thermal analysis in a DTA/DSC. This was done to confirm the identity of the exothermic events observed between 940 and 990°C. Fig. 12 is a graph of the combined, normalized XRD spectra for quenched mullite composition glass beads before and after thermal analysis. The spectrum for specimen Q was a broad, diffuse hump characteristic of amorphous materials, with a maximum near the 100% peak for crystalline mullite. Additionally, the presence of some crystalline phase was also apparent. The pattern for specimen M2 was much more crystalline. It was similar to the equilibrium mullite structure (PDF 15-1776), except that the 120 and 210 peaks overlapped (i.e. pseudotetragonal). No other phases were observed, and specifically, there was no indication of an Al–Si spinel phase. It was concluded that the exothermic events observed by DSC were due

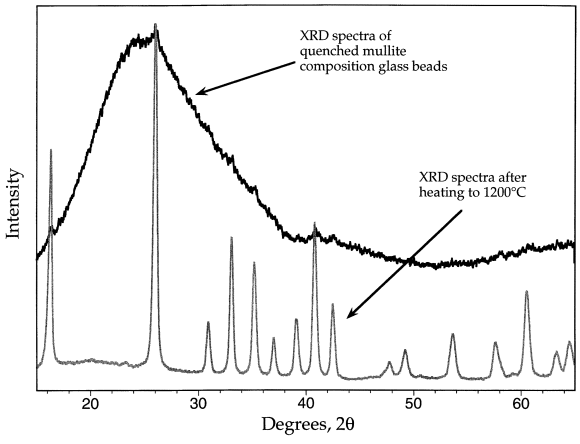

Fig. 12. Combined, normalized XRD spectra for quenched mullite composition glass beads, before and after crystallization in a DTA. The crystalline pattern was for pseudotetragonal mullite, and was proof that the exothermic events observed by DTA/DSC were due to mullite crystallization.

to mullite crystallization, since that was the only phase detected by XRD of annealed specimens.

3.4. Synchrotron powder diffraction measurements

Specimens M1, M2, M3 and M4 were chosen for Rietveld analysis using synchrotron radiation XRD data to characterize the crystal structure of mullite after various thermal treatments. One of the objectives was to determine if the multiple crystallization events observed by DSC could be validated by the presence of multiple crystalline phases in pseudotetragonal mullite. The other objective was to ascertain the crystallization pathway for quenched mullite glass by correlating microstructural results with precise crystal structure data.

3.4.1. Structure models

Mullite, a solid solution of Al_2O_3 and SiO_2, may be represented by the following general formula:

$$Al_{4+2x}Si_{2-2x}O_{10-x} \quad (5)$$

The end members of this general formula are represented by the mineral sillimanite ($x = 0$) and a hypothetical substance iota-alumina ($x = 1$). Metastable mullite with a composition of $2Al_2O_3{\cdot}SiO_2$ ($x = 0.40$) is often termed "fused mullite", since it is typically formed from the melt, whereas mullite with a composition of $3Al_2O_3{\cdot}2SiO_2$ ($x = 0.25$), such as the Kyoritsu KM101 mullite used in this study, is typically called "stoichiometric" or stable mullite. In the "average" structure model of mullite, as assigned by Bumham,[62,63] and later confirmed by Saalfeld and Guse[64] and Angel and Prewitt,[7] the repartition of the atoms on the respective Wyckoff positions within space group Pbam (No. 55) is given in Table 5. The structures of sillimanite and mullite consist of chains of edge-shared AlO_6-octahedra running parallel to the caxis that are interconnected by double chains of AlO_4/SiO_4 tetrahedra that are also parallel to the c-axis. In sillimanite, the regular AlO_4/SiO_4 tetrahedral sequence parallel to the c-axis results in a doubled c-cell. This regularity is lost in mullite, because with increasing x, Si^{4+} cations are replaced by Al^{3+} according to the reaction:

$$2Si^{4+} + O^{2-} = 2Al^{3+} + V_{\ddot{O}} \quad (6)$$

The AlO_6-octahedra are built up by Al ions at the 2a sites and oxygen atoms at O_{ab} and O_d sites. For sillimanite, the tetrahedral Al^{3+}/Si^{4+} ions occupy the T positions, whereas for mullite, any Al atom in excess of 4 replaces a Si atom at the 4h site, resulting in an oxygen vacancy at the tetrahedral corner sharing position O_c. This leads to a local structural rearrangement shifting the excess Al atom on to a new position T* and the corresponding next neighbor oxygen on to the shifted position O_c*. Fig. 13 shows projections of the idealized structures of sillimanite and mullite on to the ab-plane.

The difference between various mullites is known to manifest itself by variations of the cell dimensions and, structurally speaking, essentially by variations of the positions and occupancies of the T* and O* positions. The maximum oxygen deficiency possible by this one parameter disordered model as given by Eq. (5) and Table 5, is reached for $x = 2/3$, when all O_c atoms have been eliminated. Fischer et al.[11,12] discussed structure models for $x > 2/3$. Angel et al.[5] further refined this "average" mullite structure by assigning atoms to the T, O_{ab} and O_d positions, and by including anharmonic temperature factors. Angel et al.[5,7] also discuss the incommensurate modulations observed with certain mullites.

3.4.2. Single phase Rietveld refinement

Table 6 summarizes the results of single phase Rietveld refinements of the "low temperature" (LT) samples M1, M2 and the "high temperature" (HT) samples M3, M4 after applying the structure model and the constraints given in Table 5. The last column lists the X-ray single crystal results of Saalfeld and Guse[64] obtained from a 3:2 mullite for comparison. A remarkable qualitative difference between the LT- and HT-data is given by the large high angle line broadening (wide peaks) of the LT specimens as shown in Fig. 14. This effect is normally indicative of microstrain in the sample and it may also be responsible for the larger estimated standard deviations (esd's) of the refined LT specimen parameters. (Microstrain is a type of internal strain that refers to a situation where there is a distribution function of atomic positions in the unit cell, instead of a single, fixed, exact position for every atom, as is found in a perfect unit cell. The average of this distribution function, however does not change from the un-strained case, since there is not a net displacement of atoms. Macrostrain, on the other hand, refers to a situation where there is a net change in

Table 5
Wyckoff positions, coordinates and names[6] of the atom sites of the "average" mullite structure, space group Pbam (No. 55)

Atoms	Al_2	$[Al_2Si_{2-2x}]$	Al_{2x}	O_{2-3x}	O_{2x}	O_4	O_4
Wyckoff positions	2 a	4 h	4 h	2 d	4 h	4 h	4 g
Coordinates	0, 0, 0	x, y, _	x, y, _	_, 0, _	x, y,_	x, y, _	x, y, 0
Names[6]	Al	T(Si/Al)	T*(Al*)	O_c	O_c*	O_{ab}	O_d

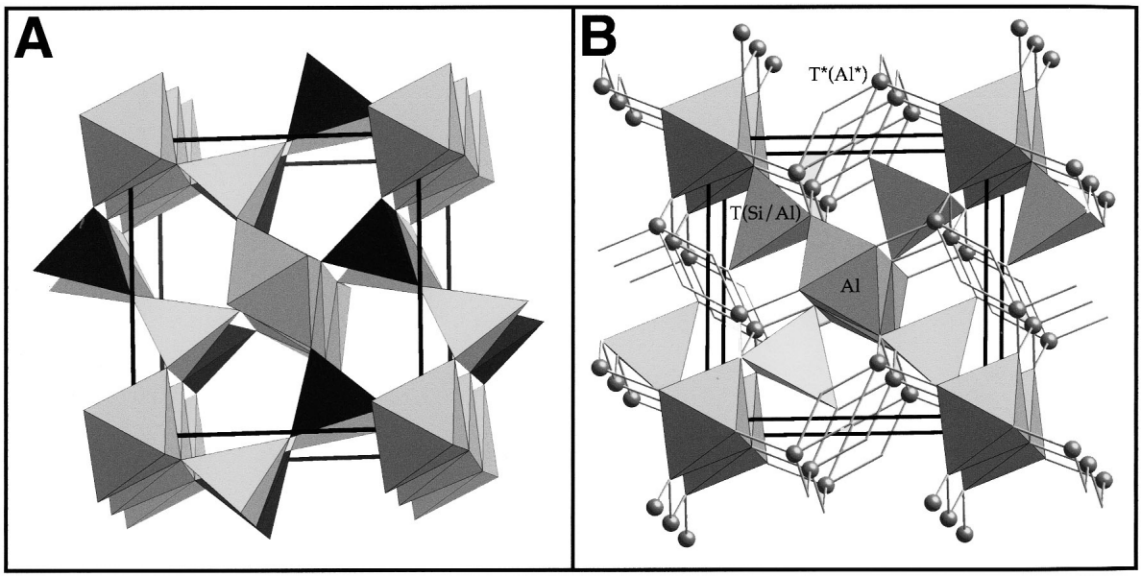

Fig. 13. Idealized structures of sillimanite (A) and mullite (B) projected along the a–b plane.

the unit cell parameters.) The microstrain indicated by line broadening from Rietveld analysis of XRD spectra (shown in Fig. 14 for M1 and M2), correlates very well with the observed strained or distorted crystal microstructure observed by TEM (e.g. variegated diffraction contrast in BF mode in Figs. 5– 9 and 11). This provides further evidence that the structure of pseudotetragonal mullite was highly strained. Additional confirmation that the strain was not an artifact of sample preparation lies in the much broader line widths for M1 and M2 as compared to M3, even though they were all prepared the same way. The refined lattice parameters for these specimens may be analyzed with respect to three criteria: (i) Al_2O_3/SiO_2 ratio, (ii) cell dimensions, and (iii) structure.

3.4.2.1. Al_2O_3/SiO_2 ratio. The most direct indicator of the Al_2O_3/SiO_2 ratio is the mixing parameter x [see Eq. (5) and the line "mullite x" in Table 6] as derived from the refined site occupancies. Due to the low X-ray scattering power of oxygen and the very low scattering contrast of Al^{3+}/Si^{4+} ions, this parameter is normally not easily refineable from powder data. However, the various site constraints (occupancies of T-, T*-, O_c- and O_c*-sites constrained by only one parameter x, isotropic temperature factors, and temperature factors of all O-atoms constrained to be identical) and the high quality of synchrotron powder data reduced the usual number of correlations between occupancies and temperature factors. The mixing parameters of the HT samples (0.34, 0.33) refined to values somewhat between the nominal values of $x = 0.25$ for 3:2 mullite and $x = 0.40$ for 2:1 mullite, whereas the value $x = 0.274$ obtained by Saalfeld and Guse[64] is much closer but still above the value for 3:2 mullite. However, the mixing parameters of the LT specimens (0.50, 0.58) refined to much higher values, even higher than the $x = 0.40$ for 2:1 mullite.

To cross-check these results obtained from Rietveld refined intensities constrained by the above structure model, three other indicators of the Al_2O_3 content were evaluated: the linear dependence of the a-lattice parameter on the Al_2O_3 content as observed by Cameron[9] and confirmed by Ban and Okada,[10] the linear dependence of the density on the composition x assuming a constant number of cations of $Al + Si = 6$ (Cameron[9]) per unit cell and the linear dependence of the ratio of the 220 and 111 reflection intensities on x (Ban and Okada[10]). Using the respective regressions:

$$Al_2O_3(\text{mol\%}) = 1443(\text{length of a axis}) - 1028.06 \quad (7)$$

$$\text{density} = -0.303 * x + 3.247 \quad (8)$$

$$Al_2O_3(\text{mol\%}) = 41.77(I_{220}/I_{111}) + 27.6 \quad (9)$$

the resulting Al_2O_3 contents are shown in Table 7. In converting the mixing parameter x to Al_2O_3 (mol.%) the obvious relations

$$Al/Si = (2 + x)/(1 - x) \text{ and } Al_2O_3(\text{mol\%}) = (2 + x)/(4 - x) \quad (10)$$

were used. We observed that the HT specimens and the literature data yielded fairly consistent Al_2O_3 contents, around 61 mol% (nominal value for 3:2 mullite: 60.0 mol%), while the LT specimens yield much higher Al_2O_3 contents, around 70 mol% (nominal value for 2:1 mullite: 66.7 mol%). Additionally, the calculated Al_2O_3 content for the LT specimens varied significantly

Table 6
Refined parameters of 4 mullite samples and a reference. Space group Pbam

Sample	M1	M2	M3	M4	Saalfeld and Guse[64]
a (nm)	0.7616 (2)	0.7606 (1)	0.75454 (2)	0.75499 (3)	0.7553 (1)
b (nm)	0.7678 (2)	0.7682 (1)	0.76956 (2)	0.76883 (3)	0.7686 (1)
c (nm)	0.28891 (4)	0.28871 (4)	0.288398 (6)	0.288379 (9)	0.28864 (7)
V (nm^3)	0.16897	0.16870	0.16746	0.16739	0.16756
Density (g/cm^3)	3.10	3.09	3.15	3.16	3.16
R_{WP}	0.049	0.049	0.051	0.032	
R_{Bragg}	0.060	0.063	0.049	0.025	0.027
X(Al)	0.0	0.0	0.0	0.0	0.0
Y(Al)	0.0	0.0	0.0	0.0	0.0
Z(Al)	0.0	0.0	0.0	0.0	0.0
B(Al)	0.9 (3)	1.0 (3)	0.5 (1)	0.5 (1)	
Occ.(Al)	1.0	1.0	1.0	1.0	1.0
X(T)	0.148 (2)	0.147 (2)	0.1480 (6)	0.1474 (6)	0.1485
Y(T)	0.339 (2)	0.340 (1)	0.3412 (6)	0.3410 (6)	0.3411
Z(T)	0.5	0.5	0.5	0.5	0.5
B(T)	1.7 (4)	0.8 (3)	0.3 (1)	0.3 (1)	
Occ.(T), Al	0.5	0.5	0.5	0.5	0.5
Occ.(T), Si	0.25 (2)	0.21 (2)	0.332 (7)	0.334 (7)	0.363
X(T*)	0.275 (4)	0.282 (4)	0.275 (3)	0.268 (3)	0.2621
Y(T*)	0.195 (4)	0.194 (4)	0.209 (2)	0.207 (2)	0.2057
Z(T*)	0.5	0.5	0.5	0.5	0.5
B(T*)	0.1 (4)	3 (1)	1.7 (8)	1.2 (8)	
Occ. (T*), Al	0.25 (2)	0.29 (2)	0.168 (7)	0.166 (7)	0.137
$X(O_{ab})$	0.354 (2)	0.349 (1)	0.3567 (6)	0.3566 (6)	0.3579
$Y(O_{ab})$	0.423 (2)	0.422 (1)	0.4195 (6)	0.4201 (6)	0.4221
$Z(O_{ab})$	0.5	0.5	0.5	0.5	0.5
$B(O_{ab})$	0.2 (2)	0.4 (2)	0.8 (1)	0.8 (1)	
$Occ.(O_{ab})$	1.0	1.0	1.0	1.0	1.0
$X(O_d)$	0.136 (2)	0.133 (1)	0.1270 (9)	0.1263 (9)	0.1265
$Y(O_d)$	0.220 (2)	0.222 (1)	0.2219 (8)	0.2216 (8)	0.2201
$Z(O_d)$	0.0	0.0	0.0	0.0	0.0
$B(O_d)$	0.2 (2)	0.4 (2)	0.8 (1)	0.8 (1)	
$Occ.(O_d)$	1.0	1.0	1.0	1.0	1.0
$X(O_c)$	0.5	0.5	0.5	0.5	0.5
$Y(O_c)$	0.0	0.0	0.0	0.0	0.0
$Z(O_c)$	0.5	0.5	0.5	0.5	0.5
$B(O_c)$	0.2 (2)	0.4 (2)	0.8 (1)	0.8 (1)	
$Occ.(O_c)$	0.26 (1)	0.58 (3)	0.49 (1)	0.50 (1)	0.590
$X(O_c*)$	0.442 (8)	0.457 (6)	0.453 (5)	0.451 (5)	0.4507
$Y(O_c*)$	0.039 (9)	0.029 (8)	0.049 (5)	0.048 (5)	0.0518
$Z(O_c*)$	0.5	0.5	0.5	0.5	0.5
$B(O_c*)$	0.2 (2)	0.4 (2)	0.8 (1)	0.8 (1)	
$Occ.(O_c*)$	0.25 (1)	0.29 (2)	0.168 (7)	0.166 (7)	0.137
Mullite x	0.49 (4)	0.58 (3)	0.34 (1)	0.33 (1)	0.274

depending on which indicator was used. This was another indication of the anomalous behaviour of the LT specimens (to be discussed in more detail below).

3.4.2.2. Cell dimensions. Fig. 15 compares the Rietveld refined cell dimensions a and c with the lines separating orthorhombic mullite from pseudotetragonal mullite as given by Cameron[9] and Ban et al.[10] The LT specimens M1 and M2 clearly fall into the region of pseudotetragonal mullite and the HT specimens M3 and M4, along with the results of Saalfeld and Guse[64] and PDF 15-776 lie within the orthorhombic mullite region. The density calculated from the refined cell dimensions increased by about 1.6% in transforming from the LT to the HT mullites. This seemed reasonable in considering that pseudotetragonal mullite is a metastable transitional phase between the amorphous starting material and the stable stoichiometric 2:1 or 3:2 mullites, and that the transition involves crystallization of the residual amorphous phase. However, this densification is brought about by a non-uniform shrinkage of the unit cell: $da/a = -0.93\%$, $db/b = +0.23\%$, $dc/c = -0.18\%$ (from M1 to M3). Since the cell dimensions of the HT specimens closely correspond to equilibrium 3:2

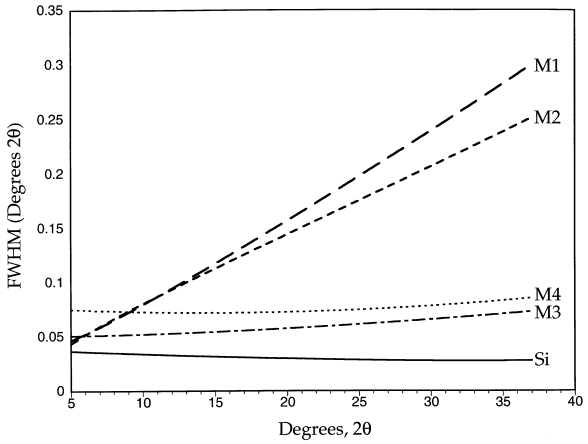

Fig. 14. Line widths, full width at half maximum (FWHM) of XRD peaks obtained from single phase Rietveld refinements of synchrotron XRD spectra for specimens M1, M2, M3, M4 and from a Si powder standard (SRM 640b, NIST). The steeper slope for M1 and M2 was an indication of microstrain in these specimens.

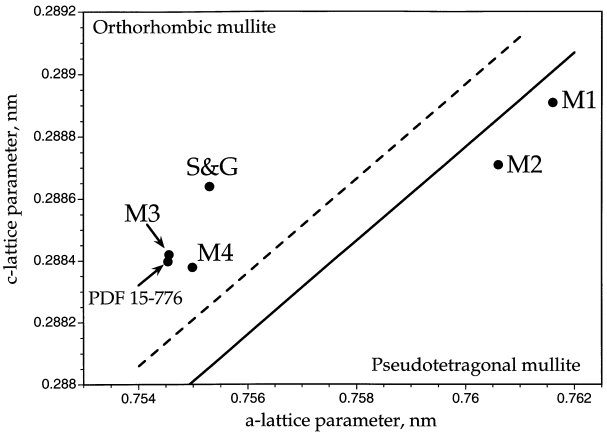

Fig. 15. Positions of the refined a and c cell dimensions for specimens M1, M2, M3 and M4 on an orthorhombic-pseudotetragonal mullite diagram. The dashed line was taken from Cameron's data,[9] the solid line from Ban and Okada's data,[10] and S&G was plotted from Saalfed and Guse's results.[64]

Table 7
Al_2O_3 contents as derived from various indicators: cell dimensions a, b, and c, density *Dx*, ratio of the integrated intensities of 220 and 111 reflections, Rietveld refined "mullite *x*" and microprobe (μ-probe)

Specimen	M1	M2	M3	M4	Saalfeld and Guse[64]
Mol% (a)	70.9	69.5	60.7	61.4	61.8
Mol% (b)	70.9	68.5	60.0	64.6	66.0
Mol% (c)					
Mol% (*Dx*)	70.8	72.3	62.8	61.8	61.8
Mol% ($I_{220/111}$)	75.2	64.9	62.5	59.9	
Mol% (mullite *x*)	71.4	75.4	63.8	63.6	61.0
Mol% (μ-probe)					60.9

mullite,[10] this implies that there is a significant amount of macrostrain imposed on metastable, alumina-rich, psuedotetragonal mullite as it transforms into equilibrium, orthorhombic 3:2 mullite. This macrostrain (net anisotropic change in unit cell parameters) is in addition to the severe amount of microstrain (distribution of atomic positions within the unit cell) that already exists in this material.

3.4.2.3. Structure. Table 6 shows that the refined structural parameters for the HT specimens agree within one estimated standard deviation (except *x*(T*), 2 esd's). This proves that specimen M3 has regained the structure of the starting material, M4. Compared to the single crystal data of Saalfeld and Guse,[64] these specimens show a slight increase towards the values of Angel et al.[5,6] obtained for 2:1 mullite.

The refined occupancies demonstrate that the transition from pseudotetragonal mullite to orthorhombic mullite is accompanied by a depopulation of Al-atoms at the T*-site in favor of an increase of Si atoms at the "normal" T-site. The corresponding depopulation of the O_c*-site in favor of an increase of the population at the "normal" O_c-site was also observed (except for sample M2), and is required by the structural model given in Eq. (5) and Table 5.

Significant changes of the positional parameters were observed in the transformation from pseudotetragonal to orthorhombic mullite. This is mostly seen by an increase of the y-coordinates of the T*- and the O*-sites, which may be related to the increase of the b-lattice parameter. A significant decrease of the x-coordinate of the octahedral O_d-oxygen may be related to the decrease of the a-lattice parameter. The other coordinates, in particular those of the T-sites and the O_{ab}-sites, remain essentially constant.

3.4.3. Multiphase Rietveld refinement

Considering the fact that specimens M1, M2 and M3 had undergone various thermal treatments, they should reflect the time-wise integrated history of their respective kinetic processes. In addition, as previously mentioned, specimen M2 was an averaged sample, consisting of a mixture of several powders with different thermal treatments, each with an ultimate temperature of 1200°C. Thus, the various thermal histories, as well as the fact that two exothermic events were observed during DSC crystallization experiments, prompted an investigation for multiple mullite phases in specimens M1 and M2. The presence of multiple phases would also help to explain the anomalously broad line (peak) widths observed in the synchrotron XRD spectra for these specimens. A close inspection of weak high angle reflections revealed overlapping peaks and shoulders that were averaged over in the single phase Rietveld refinement previously discussed. Fig. 16A is an enlarged view of the synchrotron XRD spectra around the 002 reflection for specimen M1 (crystallized at 938°C, 2.5 h). The data clearly shows

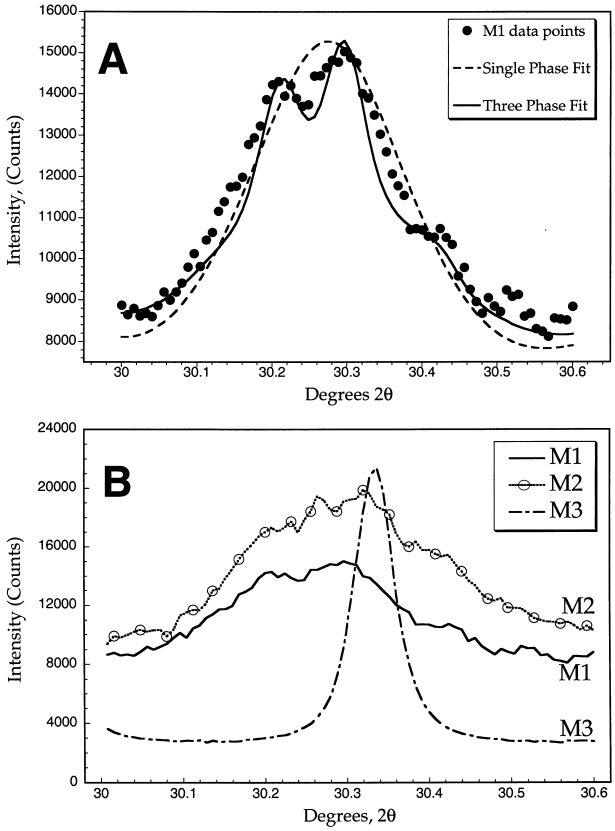

Fig. 16. Detailed portions of synchrotron XRD spectra around the well separated 002 reflection for various powder specimens. (A) Specimen M1: observed data points (dots), single phase Rietveld refinement (dashes), 3-phase Rietveld refinement (line). (B) Comparison of data from partly crystallized specimens M1, M2 with those of the well crystallized specimen M3 (scaled down by 40%). Note that there are multiple, overlapping peaks observable in the spectra of specimens M1 and M2, in contrast to the very narrow, single peak for specimen M3.

the overlap of three different peaks, indicating the presence of three different composition mullite phases. This corroborates the multiple exothermic peaks observed by DSC. The dashed line shows the results for the single phase refinement previously discussed, and the solid line the results for a three phase refinement.

An independent refinement of structure, line width, and unit cell parameters for the three phase case was not possible due to the high degree of line (peak) overlap throughout most of the spectrum. Therefore, the structure parameters for the single phase refinement were held fixed along with the narrow line width parameters taken from specimen M3. The unit cell parameters were determined from the distinct overlapping peaks observed in the 002 reflection. Three different c-cell dimensions were identified from these peaks, and the corresponding a- and b- cell dimensions (and respective Al_2O_3 mole fractions) were taken from the interpolation of the curve by Fischer et al.[11] The results are listed in Table 8. Quantitative analysis via refinement of only the scale factors yielded the indicated weight fractions. Besides the

Table 8
Results from quantitative three phase analysis of specimen M1

Parameter	Phase A	Phase B	Phase C
a (nm)	0.7651	0.7611	0.7562
b (nm)	0.7659	0.7678	0.7692
c (nm)	0.2895	0.2887	0.2875
Mol% Al_2O_3	76	70	<60
Weight fraction (%)	40	50	10

majority phase (50 wt.%) of some 70 mol% Al_2O_3, which is close to the average value obtained with the single phase analysis, a second (40 wt.%) fraction of very high Al_2O_3 content (76 mol%) and a third phase (10 wt.%) of very low Al_2O_3 content (<60 mol% Al_2O_3) was clearly identified. The c-lattice dimension (0.2875 nm) of the latter fraction is lower than observed before in any mullite, which may be related to the phenomenon of anomalously low c cell dimensions in mullites heat treated below 1200°C, as observed by Ban et al.[10,19] Additional shoulders and peak broadening at high and low angle tails of the 002 reflection (Fig. 16A) suggested that further minority phases and also microstrain were present. Fig. 16B is a plot of synchrotron XRD spectra comparing the 002 reflection region for specimens M1 (93 8°C), M2 (1200°C) and M3 (1400°C). It is apparent that a weighted distribution of at least 5–6 phases could be applied to the 002 peak for specimen M2. The very narrow 002 reflection for specimen M3 shows the final product phase after the tetragonal-orthorhombic transition was completed.

The multiple peaks in M1 and M2 at the low angle side (high c-cell dimension, high Al_2O_3 content), as well as on the high angle side (low c-cell dimension, low Al_2O_3 content), of the final 002 reflection position of sample M3, suggest the following picture of the crystallization sequence: At the beginning two phases of high and low Al_2O_3 content respectively start to crystallize, obviously because of the miscibility gap discussed by Ban et al.[57] and Takei et al.[58] With time and temperature these transform into the final phase as determined by the bulk Al_2O_3 and SiO_2 composition. It should be mentioned that the starting phase with the very high Al_2O_3 content (76 mol%) is very close to the composition of 78 mol%, where Fischer et al.[11] placed the crossover point of the a- and b-cell dimensions, i.e. close to the ideal "tetragonal" mullite. However, even at this composition the structure remains orthorhombic with a symmetrically independent coincidence of a and b. It should also be mentioned, that according to the one parameter structure model [Eq. (5)] and Table 5, the composition $x = 2/3$, where all of the O_c oxygen atoms are replaced by vacancies, corresponds to only slightly higher Al_2O_3 content of 80 mol%. This suggests that the "tetragonal" mullite with a quasi equal distribution of O_c-vacancies along the a- and b-cell directions has the

lowest lattice energy and thus crystallizes first. Only subsequent annealing produces Si/Al exchange coupled with placing O_c oxygens onto their vacant sites. This process seems to occur preferentially along the a-cell direction leading to the inverse change in length of a and b.

Summarizing, we may state that the synchrotron XRD spectra for specimens M1 and M2 reflect integrated time histograms of incomplete mullite crystallization that show the formation of multiple mullite phases. To reduce the observed heavy line overlap, in situ (isothermal) high temperature and high resolution powder diffraction experiments should be performed to follow the structural implications of the crystallization pathway and kinetics in more detail.

Although the thermal history of specimens M1 and M2 were different (single sample heated at 938°C for 2.5 h, vs. a mixture of powders annealed at different temperatures and heated at different rates to a maximum temperature of 1200°C), the composition and structure of these specimens (as determined by Rietveld analysis of synchrotron XRD spectra) were somewhat similar (Tables 6 and 7). These similarity reflects the time and temperature dependence of the gradual pseudotetragonal to orthorhombic transition. The fact that detailed analysis of the 002 peak for specimen M2 (a mixture of powders) showed evidence of 5 or 6 different overlapping mullite phases, was also consistent with a gradual, thermally activated, transition. The variations in microstructure for these specimens (M1, M1.5 and M2, Table 4) also demonstrate this type of transition. Consequently, it would be reasonable to expect that if a series of specimens were annealed at 1200°C for different lengths of time, a gradual variation in lattice parameters and composition of mullite crystals would probably be observed. This type of experiment was not done, however, since this phenomenon has already been reported[3,8,10,14,65] and the kinetics of this transition have also been calculated.[53]

5. Summary

1. Pseudotetragonal mullite was observed to crystallize directly from $3Al_2O_3{\cdot}2SiO_2$ composition quenched melts between 920 and 990°C, without the formation of intermediate phases such as Al–Si spinel. This was identified as the first stage of mullite crystallization. The kinetics for initial crystallization of pseudotetragonal mullite were characterized by DSC as a two-step process, with activation energies of 892 and 1333 kJ/mol for the two steps, respectively. The presence of multiple crystalline phases was confirmed by Rietveld analysis of synchrotron XRD data for specimens crystallized at low temperatures. Multiple Rietveld phase fitting (3 phases) was successfully applied to a specimen isothermally crystallized at 938°C for 2.5 h. Phase separation in the quenched melts and during subsequent heating was suggested as the reason for multiple phases being formed.

2. Crystallization of pseudotetragonal mullite occurred via a nucleation and growth process without an induction period. Quenched mullite composition glasses were observed to be site saturated with discrete, ellipsoidal, crystallites ($\sim 13.5 \times 11.5$ nm) throughout the bulk after being annealed at 920°C for 3 h. The crystallites coalesced and grew three-dimensionally with apparent spherulitic grain growth. The computed Avrami exponent, $n = 3.23$, was consistent with the observed microstructure ($n = 3$ for three dimensional, bulk, crystal growth). Crystallization was observed to occur rapidly at temperatures above 970°C when heated at moderate rates (3.0–10.0°C/min).

3. Pseudotetragonal mullite specimens had a microstructure of faceted, angular grains $\sim 200 \times 300$ nm in size with numerous small $\sim 7 \times 10$ nm inclusions embedded within them. The pseudotetragonal mullite crystals contained a large amount of internal strain (microstrain) as observed by the variegated contrast in BF TEM micrographs and by the broad high-angle peaks in the synchrotron XRD spectra. The strain was spatially correlated to the embedded inclusions.

4. Rietveld analysis of synchrotron XRD spectra for $3Al_2O_3{\cdot}2SiO_2$ composition mullite glass crystallized at temperatures $\leqslant 1200$°C determined that the crystals were pseudotetragonal with a composition of approx. 70 mol% Al_2O_3 (based on their lattice parameters). Multiple phases were detected. The formation of the Al_2O_3-rich phases was attributed to phase separation as a result of a metastable immiscibility gap. The XRD spectra for these specimens contained a large amorphous background. Since the initial composition of the glass was 60 mol% Al_2O_3, and the crystals contained 70 mol% Al_2O_3, it was inferred that there was a SiO_2-rich, amorphous phase also present in the material.

5. Quantitative Rietveld fitting of high angle pseudotetragonal mullite peaks (002) suggested that a "tetragonal" (symmetrically independent coincidence of a- and b- lattice parameters) mullite, with a quasi-equal distribution of O_c vacancies along the a- and b-cell dimensions, had the lowest free energy, and that it was first phase to crystallize. Subsequent annealing was suggested to produce Si/Al exchange, coupled with placing oxygens onto vacant O_c sites. This process appeared to occur preferentially along the a-cell direction, leading to the inverse change in the length of a and b as the pseudotetragonal phase converted to the orthorhombic phase.

6. Direct TEM characterization of nm-sized inclusions, embedded in pseudotetragonal mullite crystals, was complicated by their small size, sensitivity to beam damage, and chemical similarity to the matrix. Based on SAD and EDS, it was inferred that they were amorphous and differed in composition from the matrix. Coupled with the existence of an amorphous, SiO_2-rich phase (as deduced

from XRD spectra and Rietveld analysis),it was concluded that the inclusions were amorphous and rich in SiO_2.

7. During the second stage of mullite crystallization, from 1000 to 1200°C, slight changes were observed in the microstructure of pseudotetragonal mullite. This stage was characterized by the gradual assimilation of the 7–10 nm, SiO_2-rich inclusions, and a reduction in grain size, as the spherulitic grains started to segment. Between 938 and 1200°C, there was an approx. 22% reduction in the size of the inclusions, and an approx. 27% reduction in grain size. Additionally, the composition of the pseudotetragonal mullite crystals was closer to that of the bulk material (based on the $I_{220/111}$, intensity ratio).

8. During the third stage of mullite crystallization, from 1200–1400°C, the conversion of pseudotetragonal mullite to orthorhombic mullite was completed, as determined by Rietveld analysis of synchrotron XRD spectra. By 1400°C, the microstrain previously observed by Rietveld analysis was gone. Additionally the variegated contrast observed by TEM in BF mode as well as the inclusions were eliminated from many, if not most of the grains. At this temperature, equilibrium, orthorhombic mullite was formed, the material was single-phase, the composition was ~60 mol% Al_2O_3, and a more typical, polycrystalline microstructure was observed.

The pseudotetragonal– orthorhombic transition was accompanied by ~67% reduction in grain size from 1200–1400°C. Those grains that still retained inclusions and appeared strained were often surrounded by numerous, smaller, strain-free, and inclusion-free grains. This was interpreted as strain-induced recrystallization. The relief of built up internal strain from the embedded inclusions and the anisotropic change in lattice parameters from the phase transition was suggested as the driving force for creating new grains. Recrystallization after annealing highly strained metals was offered as an example of a similar phenomenon.

Acknowledgements

The authors would like to gratefully acknowledge Richard Weber and Johan Abadie from Containerless Research Inc. for supplying the quenched mullite beads used in this work; Pankaj Sam from the University of Illinois and Paul Zschack from the UNICAT facility at the APS facility at ANL for their assistance in collecting the synchrotron radiation data; and Ray Twesten from the University of Illinois, for his suggestions regarding microstructural analysis. This project was funded by the US Air Force Office of Scientific Research under Science and Technology Transfer Research (STTR) grants F49620-97-l-0427 and F49620-98-C-0050. Microstructural and crystallographic characterization was performed in part using equipment in the Center for Microanalysis of Materials (in the Materials Research Laboratory) and in the Center for Cement Composite Materials, both located at the University of Illinois at Urbana Champaign. The UNICAT facility located at the Advanced Photon Source (APS) is supported by the University of Illinois at Urbana-Champaign, Materials Research Laboratory (U.S. Department of Energy, the State of Illinois-IBHE-HECA and the National Science Foundation), the Oak Ridge National Laboratory (U.S. Department of Energy under contract with Lockheed Martin Energy Research), the National Institute of Standards and Technologies (U.S. Department of Commerce) and UOP LLC. The APS is supported by the U.S. Department of Energy, BES, Office of Energy Research under contract No. W-31-109-ENG-38.

References

1. Kriven, W. M. and Pask, J. A., Solid solution range and microstructures of melt-grown mullite. *J. Am. Ceram. Soc.,* 1983, **66**(9), 649–654.
2. Prochazka, S. and Klug, F. J., Infrared-transparent mullite ceramic. *J. Am. Ceram. Soc.,* 1983, **66**(12), 874–880.
3. Okada, K. and Otsuka, N., Change in chemical compostion of mullite formed from $2SiO_2{\cdot}3Al_2O$ xerogel during the formation process. *J. Am. Ceram. Soc.,* 1987, **70**(10), C245–C247.
4. Rahman, S. H., Crystal chemistry of mullite. In *Mullite and Mullite Ceramics*, ed. H. Schneider, K. Okada and J. Pask. John Wiley and Sons, New York, 1994, pp. 5–82.
5. Angel, R. J., McMullan, R. K. and Prewitt, C. T., Substructure and superstructure of mullite by neutron diffraction. *Am. Mineral.,* 1991, **76**, 332–342.
6. Angel, R. J. and Prewitt, C. T., Crystal structure of mullite: a re-examination of the average structure. *Am. Mineral.,* 1986, **71**, 1476–1482.
7. Angel, R. J. and Prewitt, C. T., The incomensurate structure of mullite by Patterson synthesis. *Acta Crystallogr.,* 1987, **B43**, 116–125.
8. Wang, Y. and Thomson, W. J., Mullite formation from non-stoichiometric slow hydrolyzed single phase gels. *J. Mater. Res.,* 1995, **10**(4), 912–917.
9. Cameron, W. E., Composition and cell dimensions of mullite. *Am. Ceram. Soc. Bull.,* 1977, **56**(11), 1003–1011.
10. Ban, T. and Okada, K., Structure refinement of mullite by the Rietveld method and a new method for estimation of chemical composition. *J. Am. Ceram. Soc.,* 1992, **75**(1), 227–230.
11. Fischer, R. X., Schneider, H. and Schmucker, M., Crystal structure of Al-rich mullite. *Am. Mineral.,* 1994, **79**(9-10), 983–990.
12. Fischer, R. X., Schneider, H. and Voll, D., Formation of aluminum rich 9:1 mullite and its transformation to low alumina mullite upon heating. *J. Eur. Ceram. Soc.,* 1996, **16**, 109–113.
13. Osaka, J., Tetragonal mullite-like phase from co-precipitated gels. *Nature,* 1961, **191**, 1000–1001.
14. Li, D. X. and Thomson, W. J., Tetragonal to orthorhombic transformation during mullite formation. *J. Mater. Res.,* 1991, **6**(4), 819–824.
15. Schneider, H. and Rymon-Lipinski, T., Occurrence of pseudotetragonal mullite. *J. Am. Ceram. Soc.,* 1988, **71**(3), C162–C164.
16. Schneider, H., Fischer, R. X. and Voll, D., Mullite with lattice constants a > b. *J. Am. Ceram. Soc.,* 1993, **76**(7), 1879–1881.

17. Petry, M. D. and Tai-Il, M., Effect of thermal exposures on the strengths of Nextel™ 550 and 720 filaments. *J. Am. Ceram. Soc.,* 1999, **82**(10), 2801–2807.
18. Okada, K., Hoshi, Y. and Otsuka, N., Formation reaction of mullite from SiO_2–Al_2O_3 xerogels. *J. Mater. Sci. Lett.,* 1986, **5**(12), 1316–1318.
19. Ban, T. and Okada, K., Analysis of local cation arrangement in mullite using ^{29}Si magic-angle spinning nuclear magnetic resonance spectra. *J. Am. Ceram. Soc.,* 1993, **76**(10), 2491–2496.
20. Tkalcec, E., Nass, R., Schmauch, J., Schmidt, H., Kurajica, S., Bezjak, A. and Ivankovic, H., Crystallization kinetics of mullite from single-phase gel determined by isothermal differential scanning calorimetry. *J. Non-Cryst. Solids,* 1998, **223**, 57–72.
21. Wei, W.-C. and Halloran, J. W., Phase transformation of diphasic aluminosilicate gels. *J. Am. Ceram. Soc.,* 1988, **71**(3), 166–172.
22. Wei, W.-C. and Halloran, J. W., Transformation kinetics of diphasic aluminosilicate gels. *J. Am. Ceram. Soc.,* 1988, **71**(7), 581–587.
23. Boccaccini, A. R., Khalil, T. K. and Bucker, M., Activation energy for the mullitization of a diphasic gel obtained from fumed silica and boehmite sol. *Mater. Lett.,* 1999, **38**(2), 116–120.
24. Okada, K., Otsuka, N. and Osaka, J., Characterization of spinel phase formed in the kaolin-mullite thermal sequence. *J. Am. Ceram. Soc.,* 1986, **69**(10), C251–C253.
25. Okada, K. and Otsuka, N., Characterization of the spinel phase from SiO_2–Al_2O_3 xerogels and the formation process of mullite. *J. Am. Ceram. Soc.,* 1986, **69**(9), 652–656.
26. Hyatt, M. J. and Bansal, N. P., Phase transformations in xerogels of mullite composition. *J. Mater. Sci.,* 1990, **25**(6), 2815–2821.
27. Chakraborty, A. K., Formation of silicon-aluminum spinel. *J. Am. Ceram. Soc.,* 1979, **62**(3-4), 120–124.
28. Chakraborty, A. K., Intermediate Si–Al spinel phase formation in phase transformation of diphasic mullite gel. *J. Mater. Sci.,* 1993, **28**(14), 3839–3844.
29. Sujeong, L., Youn Joong, K. and Hi-Soo, M., Phase transformation sequence from kaolinite to mullite investigated by an energy-filtering transmission electron microscope. *J. Am. Ceram. Soc.,* 1999, **82**(10), 2841–2848.
30. Ban, T., Hayashi, S., Yasumori, A. and Okada, K., Characterization of low temperature mullitization. *J. Eur. Ceram. Soc.,* 1996, **16**, 127–132.
31. Zhu, D., Jilavi, M. H. and Kriven, W. M., Synthesis and characterization of mullite and YAG fibers grown from deeply undercooled melts. *Ceram. Eng. Sci. Proc.,* 1997, **18**(3), 31–38.
32. Kriven, W. M., Jilavi, M. H., Zhu, D., Weber, J. K. R., Cho, B., Felten, J. and Nordine, P. C., Synthesis and microstructure of mullite fibers grown from deeply undercooled melts. In *Ceramic Microstructures: Control at the Atomic Level. Proceedings of the International Materials Symposium on Ceramic Microstructures '96: Control at the Atomic Level*, ed. A. P. Tomsia and A. M. Glaeser. Plenum Press, New York, 1998, pp. 169–176.
33. Weber, J. K. R., Cho, B., Hixson, A. D., Abadie, J. G., Nordine, P. C., Kriven, W. M., Johnson, B. R. and Zhu, D., Growth and crystallization of YAG- and mullite-composition glass fibers. *J. Eur. Ceram. Soc.,* 1999, **19**(13-14), 2543–2550.
34. Weber, J. K. R., Felten, J. J. and Nordine, P. C., New method of high purity ceramic synthesis. *Rev. Sci. Inst.,* 1996, **78**, 31–35.
35. Weber, J. K. R., Anderson, C. D., Krishnan, S. and Nordine, P. C., Solidification behavior of undercooled liquid aluminum oxide. *J. Am. Ceram. Soc.,* 1995, **78**, 577–582.
36. Weber, J. K. R., Hampton, S. S., Merkley, D. R., Rey, C. A., Zatarski, M. M. and Nordine, P. C., Aero-acoustic levitation — a method for containerless liquid-phase processing at high temperatures. *Rev. Sci. Inst.,* 1994, **65**, 456–465.
37. Weber, J. K. R. and Nordine, P. C., Containerless liquid-phase processing at high temperatures. *Microgravity Science and Technology,* 1995, **VII**, 279–282.
38. Krishnan, S., Felten, J. J., Rix, J. E. and Weber, J. K. R., Levitation apparatus for structural studies of high temperature liquids using synchrotron radiation. *Rev. Sci. Inst.,* 1997, **68**, 3512–3518.
39. Benedict, J., Anderson, R. and Klepeis, S. J., Recent developments in the use of the tripod polisher for TEM specimen preparation. In *Specimen Preparation for Transmission Electron Microscopy of Materials III, Materials Research Society Symposium Proceedings,* Vol. 254, ed. R. Anderson, B. Tracy and J. Bravman. Materials Research Society, Pittsburgh, PA, 1992, pp. 121–141.
40. Klepeis, S. J., Benedict, J. P. and Anderson, R. M., A grinding/polishing tool for TEM sample preparation. In *Specimen Preparation for Transmission Electron Microscopy of Materials, Materials Research Society Symposium Proceedings,* Vol. 115, ed. J. C. Bravman, M. Anderson and M. L. McDonald. Materials Research Society, Pittsburgh, PA, 1988, pp. 179–184.
41. Williams, D. B. and Carter, C. B., *Transmission Electron Microscopy a Textbook for Materials Science*. Plenum Press, New York, 1996.
42. Bright, D. S., *Program: Maclispix, v. 2-99*. National Institute of Standards, Gaithersburg, MD, 1999.
43. Vischer, N., *Program: Object-image, v. 2.06*. University of Amsterdam, Amsterdam, The Netherlands, 2000.
44. Bansal, N. P. and Doremus, R. H., Determination of reaction kinetic parameters from variable temperature DSC or DTA. *J. Therm. Anal.,* 1984, **29**, 115–119.
45. Bansal, N. P., Doremus, R. H., Bruce, A. J. and Moynihan, C. T., Kinetics of crystallization of ZrF_4–BaF_2–LaF_3 glass by differential scanning calorimetry. *J. Am. Ceram. Soc.,* 1983, **66**(4), 233–238.
46. Bansal, N. P. and Hyatt, M. J., Crystallization kinetics of BaO-Al_2O_3-SiO_2 glasses. *J. Mater. Res.,* 1989, **4**(5), 1257–1265.
47. Ray, C. S. and Ray, D. F., Nucleation and crystallization in glasses as determined by DTA. In *Nucleation and Crystallization in Liquids and Glasses, Ceramic Transactions,* Vol. 30, ed. M. C. Weinberg. The American Ceramic Society, Westerville, Ohio, 1993, pp. 207–233.
48. Cheng, K., Determining crystallization kinetic parameters of Li_2O-Al_2O_3-SiO_2 glass from derivative differential thermal analysis curves. *Mater. Sci. Eng. B.,* 1999, **60**(3), 194–199.
49. Kissinger, H. E., Variation of peak temperature with heating rate in differential thermal analysis. *J. Res. Nat. Bur. Stand.,* 1956, **57**(4), 217–221.
50. Augis, J. A. and Bennet, J. D., Calculation of the Avrami parameters for heterogeneous solid state reactions using a modification of the Kissinger method. *J. Therm. Anal.,* 1978, **13**(2), 283–293.
51. Porter, D. A. and Easterling, K. E., *Phase Transformations in Metals and Alloys*. Chapman and Hall, New York, 1992.
52. Li, D. X. and Thomson, W. J., Kinetic mechanisms for mullite formation from sol-gel precursors. *J. Mater. Res.,* 1990, **5**(9), 963–1969.
53. Takei, T., Kameshima, Y., Yasumori, A. and Okada, K., Crystallization kinetics of mullite in alumina-silica glass fibers. *J. Am. Ceram. Soc.,* 1999, **82**(10), 2876–2880.
54. Okada, K., Ban, T. and Yasumori, A., Immiscibility phase separation in Al_2O_3–SiO_2 system and crystallization of mullite. *Eur. J. Solid State & Inorg. Chem.,* 1995, **32**, 683–692.
55. MacDowell, J. F. and Beall, G. H., Immiscibility and crystallization in Al_2O_3-SiO_2 glasses. *J. Am. Ceram. Soc.,* 1969, **52**(1), 17–25.
56. Risbud, S. H. and Pask, J. A., Calculated thermodynamic data and metastable immiscibility in the system SiO_2–Al_2O_3. *J. Am. Ceram. Soc.,* 1977, **60**(9-10), 418–424.
57. Ban, T., Hayashi, S., Yasumori, A. and Okada, K., Calculation of metastable immiscibility region in the Al_2O_3–SiO_2 system. *J. Mater. Res.,* 1996, **11**(6), 1421–1427.

58. Takei, T., Kameshima, Y., Yasumori, A. and Okada, K., Calculation of metastable immiscibility region in the Al_2O_3–SiO_2 system using molecular dynamics simulation. *J. Mater. Res.,* 2000, **15**(1), 186–193.
59. Huling, J. C. and Messing, G. L., Chemistry-crystallization relations in molecular mullite gels. *J. Non-Cryst. Solids,* 1992, **147-148**, 213–221.
60. Vlack, L. H. V., *Materials Science for Engineers.* Addison-Wesley, Reading, MA, 1970.
61. Li, D. X. and Thomson, W. J., Mullite formation kinetics of a single-phase gel. *J. Am. Ceram. Soc.,* 1990, **73**(4), 964–969.
62. Burnham, C. W., Crystal structure of mullite. *Carnegie Inst. Washington Yearbook,* 1964, **63**, 223–227.
63. Burnham, C. W., Composition limits of mullite and the sillimanite-mullite solid solution problem. *Carnegie Inst. Washington Yearbook,* 1964, **63**, 227–228.
64. Saalfeld, H. and Guse, W., Structure refinement of 3:2 mullite ($3Al_2O_3{\cdot}2SiO_2$). *Neues Jahrb. Mineral. Monatsh.*, 1981, 145–150.
65. Ruscher, C. H., Schrader, G. and Gotte, M., Infra-red spectroscopic investigation in the mullite field of composition: $Al_2(Al_{2+2x}Si_{2-2x})O_{10-x}$ with $0.55 > x > 0.25$. *J. Eur. Ceram. Soc.,* 1996, **16**, 169–175.